ATMOSPHERIC TEMPERATURE PROFILING USING ROTATIONAL RAMAN LIDAR MEASUREMENTS AND 32-CHANNEL SPECTRAL DECTECTOR

KANUPRIA SETH

A THESIS SUBMITTED TO

THE FACULTY OF GRADUATE STUDIES

IN PARTIAL FULFILMENT OF THE REQUIREMENTS

FOR THE DEGREE OF

MASTER OF SCIENCE

GRADUATE PROGRAMME IN PHYSICS AND ASTRONOMY

YORK UNIVERSITY

TORONTO, ONTARIO

MARCH 2021

Abstract

Atmospheric backscatter measurements with lidar at 355 nm laser wavelength were conducted at York University. The novel combination of the lidar system with a new 32-channel spectral detector made possible detecting photon-counting signals for multiple wavelengths simultaneously. The goal of this research was to derive atmospheric temperature profiles using the rotational Raman backscatter signal. The temperature was derived using the ratio of two wavelength intervals in the rotational Raman backscatter spectrum. A calibration function for the signal ratio and temperature on June 6, 2019 was found using temperature data from radiosonde measurements in Buffalo. The calibration function was used to derive temperature from ground up to 1200 m using lidar measurements on April 18, June 11 and June 12 in 2019. The lidar-calculated temperature profile had a mean deviation of 2.14 K from the radiosonde temperature values. The method requires improvements, such as controlling the temperature of the edge filter to minimize changes in the calibration from day to day.

Dedication

This thesis is dedicated to my parents and my sister.

Acknowledgements

I would like to thank my supervisor, Dr. James Whiteway for his support through the process of completing my MSc. Physics degree. It is an honour to work with an accomplished scientist who has contributed to some incredible breakthroughs in the area of atmospheric science and put Canada on the global map with his past work. I sincerely thank him for providing a comfortable yet driven environment with state of the art technology that helped challenge my skills and aptitude.

I would like to thank Dr. Mark Gordan for his time in reviewing my work through research evaluations and for his feedback to improve my research, along with teaching the Cloud Physics and Radar Meteorology course wonderfully. A special thank you to Dr. Matthew Johnson for brilliantly teaching the Quantum Mechanics course and his encouragement to students to learn beyond the text. His support and advice as the Graduate Program Director of Physics and Astronomy is greatly appreciated.

A big thank you to Cristal Del Biondo for her help with administrative needs and advice during my degree, and to the friendly staff at York University. Thank you to Eamonn McKernan for his help and Matlab code to read the binary data from the Licel program.

Thank you to my past supervisors, Dr. G.W.K. Moore, Dr. Kim Strong and Dr. Paul Kushner for their guidance, encouragement and teachings during my past research projects and internships in climate change science at University of Toronto.

My parents, Shuchi Seth and Amit Jit Rai Seth have made possible every aspect of my journey in Canada with their support and encouragement. A massive thank you to them for

providing everything I needed to pursue my Bachelor's and Master's degree. My sister, Gurpriya Seth has been my biggest source of strength and happiness. Thank you to my dear friends: Gurteshwar, Pankti, Saloni, Raksha, Kartik, Shivangam, Sattu, Koch, Hiba, Anjanaa, and Hamza for supporting me and standing by my side throughout. A warm thank you to Devaksh for always pushing me to do better.

Jai Hind!

Table of Contents

List of Figures

List of Tables

Chapter 1.

Introduction

This study is aimed at deriving the vertical temperature profile of the atmosphere using ground based lidar measurements of rotational Raman backscatter signal. The goal of this project is to test the novel combination of the lidar system with a 32-channel multispectral detector for temperature derivation within ± 1 K margin of relative uncertainty and absolute uncertainty.

The Earth's atmosphere impacts life on the planet directly and understanding the atmospheric parameters that influence day-to-day conditions is crucial for weather forecasting as well as for climate change projections. The distance of the upper atmosphere from humans and technology on the ground forms a major barrier in measuring the atmosphere, especially at mid and high atmospheric levels. Measuring the characteristics of the atmosphere from ground is achieved by various remote sensing methods, which can be broadly divided into passive and active remote sensing. Passive remote sensing involves measurements of electromagnetic radiation that was emitted from an atmospheric source or solar radiation that was absorbed and scattered through the atmosphere. Active remote sensing involves the emission of radiation from the instrument's own energy source and the detection of radiation scattered back from the atmosphere. Radar (radio detection and ranging) and lidar (light detection and ranging) are two examples of widely used active atmospheric remote sensing technologies. Both involve the emission of electromagnetic pulses toward the target medium and measurements of the backscatter received at the source.

Radio waves are used in radar measurements, whereas laser pulses are used in lidar technology. Invented in 1960, laser stands for light amplification by stimulated emission of radiation [*R. Gordon*, 1959]. The process involves a stimulated emission of photons having the same phase, frequency, polarisation and direction, creating laser light which is coherent and near-monochromatic.

A key parameter to gauge the state of the atmosphere is temperature, which is governed by many factors including absorption of solar radiation, emission and absorption of infrared radiation, adiabatic compression or expansion, release or absorption of latent heat, conduction, convection, and turbulent mixing. Temperature measurements are important for understanding the different natural phenomenon including atmospheric dynamics, weather variation in different locations, climatology including long-term influence of carbon on climatic conditions, meteorology, and atmospheric chemistry. Vertical atmospheric temperature profiles are required to determine other quantities varying with altitude such as the maximum water vapour pressure carrying capacity of an air parcel. The temperature at different height levels determines the stability of the atmosphere to convection, which impacts the formation of local phenomenon such as cumulus clouds, thunderstorms, and hurricanes. Therefore, the motivation to determine the vertical atmospheric temperature profile using lidar technology was its importance for multiple applications.

Different lidar methods available and under development for temperature profiling include the rotational Raman, Rayleigh, and resonance florescence. Rayleigh or elastic scattering results from electronic transitions in molecules in which the emitted photon has the same energy as the incident photon. Raman scattering results from transitions in the vibrational or rotational levels of the molecule which result in the scattered light having a shifted wavelength, which is explained in Section 2. The Rayleigh lidar method is based on assumptions of an atmospheric hydrostatic equilibrium and scattering by molecules only,

whereas the rotational Raman technique produces backscatter signal based on the total scattering occurring in the atmosphere at the time of measurements- without assumptions on the state of the atmosphere [*Behrendt et al.,* 2004]. The Rayleigh method is applicable at heights in the stratosphere and mesosphere above the aerosol and cloud layers, and uses the relative molecular number density measurements to evaluate temperature using the hydrostatic equation and the ideal gas law. With this method, a temperature profile is derived in successive steps or by integration of the molecular number density to obtain a vertical profile of pressure, starting with a known value at a reference height. Since the temperature values are found using relative number density values, it is not dependent on the normalization of the density profile. However, at heights below 25 km where aerosol particles are present in sufficient quantities, an inelastic lidar detecting backscatter such as the vibrational Raman signal from N_2 and O_2 can be used for temperature profiling [*Behrendt,* 2005]. Further, at lower altitudes where aerosol density is large and dominates the optical extinction coefficient, using vibrational Raman to quantify temperature is not accurate. Here, a rotational Raman lidar will be useful.

DIAL (Differential Absorption Lidar) is based on the same principal as an elastic backscatter lidar but it operates at two wavelengths- on and off and absorption line of the molecule of interest, such as oxygen. This method was proposed in the 1980s, although with less success in application until 2019. Since the wavelength at resonance is strongly absorbed, the difference between both the signals is proportional to the absorption by O_2 molecules. Combining two DIAL systems, one measuring temperature-sensitive O_2 absorption and other measuring the water vapour density, with a HSLR (High Spectral Resolution Lidar) measuring elastic backscatter, all in one system, has been used to effectively generate temperature profiles validated by comparison with local sounding data

[*Stillwell et al.,* 2020]. The advantage of temperature profiling using DIAL is that it does not require external calibration.

In this thesis project, pure rotational Raman scattering is used for deriving temperature from lidar measurements using a multi-spectral detector which detects the signal at different wavelengths simultaneously. The solution to the lidar equation, described in Section 3.3, for elastic scattering has been explored in many studies and most of these are derived variations of the Hitschefeld and Bordan's solution for meteorological radars initiated in 1954. James Klett presented an analytical method to invert the elastic single-scattering lidar equation using a one-component model for the total atmospheric optical extinction coefficient, without separation of the molecular and aerosol components [*Klett,* 1981]. In 1983, Fredrick Fernald further developed an inversion algorithm for the two distinct molecular and aerosol components [*Fernald,* 1984].

The conventional instrument for measuring the vertical profile of atmospheric thermodynamic parameters is the radiosonde. This is a small instrument package suspended from helium or hydrogen filled balloons and consisting of sensors that measure temperature, pressure and relative humidity. The recorded data is sent via battery-powered transmitters to ground receivers. Radiosonde includes a parachute to slow its decent back to ground to minimize hazard to property and people, and the device is often lost after the process. Lidars are useful in studying atmospheric purposes because of its unique continuity of measurements over time.

Ground-based elastic backscatter lidars are the most common type of lidar system used in atmospheric measurements and play an essential role in calibration and validation of middle-atmosphere measurements in support of other missions. Before laser light, searchlights played an important role in advancements in research in the upper atmosphere, which was distant and expensive to access. One of the first successful attempts to

characterize atmospheric temperature using lidar-like technology traces back to 1953 when L. Elterman derived a temperature profile up to 67.6 km using a ground-based searchlight technique [*Elterman,* 1953]. 'Laser radar' or lidar, was used for meteorological observations as early as in 1965 with Q-switched, ruby laser powered atmospheric measurements of clouds at the Standford Research Institute [*Northend et al.,* 1966]. In 1966, Clemesha et al. derived atmospheric temperature using lidar measurements by determining the change in scale height from 6.1 km to 7.6 km at 35 km and 45 km above ground, respectively, and relating that to a change in temperature of 52 K [*Clemesha et al.,* 1966]. Preliminary optical radar temperature measurements with inelastic signals using pioneering integration-technique were carried out by Fiocco et al. in early 1970s [*Fiocco,* 1971]. They used a Fabry-Perot interferometer to determine temperature with an accuracy of the order of a few degree Kelvin with a 2 km height averaging over 4 km. Attempts to measure temperature profiles with Cabannes scattering and using Michelson interferometer did not succeed [L*ading et al,* 1979]. Later, L. Landing proposed temperature profiling from the ratio of Rayleigh-scattered photon count signals measured using a lidar setup with two Michelson interferometers in parallel as receivers [*Lading and Schwiesow,* 1981]. At the same time, Cooney et al. (1972) conducted temperature profiling using rotational Raman signal and was one of the first to leverage the temperature information contained in the Raman spectrum. He compared two different portions of the N_2 Raman spectrum, either of the stokes or anti-stokes branch, that were received by two different optical filters in the setup to produce the temperature profile of the scattering range by optimizing the filter characteristics to maximize temperature sensitivity [*Cooney,* 1972]. This process is similar to the one employed in the research and analysis in this thesis. With the evolution of lasers in the 1960s and 1970s, the ones used for lidar measurements progressed from ruby and dye lasers to Nd: YAG and excimer lasers [*Behrendt,* 2005].

There are many commercial applications of measuring atmospheric temperature in the hydrological and agricultural industry because of the impact on crop yield and productivity of farming. Climate policies in national governments and international organizations such as the United Nations are informed by detailed research of temperature trends. Daily weather reporting is conducted by the environment department of governments, while the private sector market of weather reports and forecasts is valued at $7 billion and is growing at a rate of 10% to 15% each year [National Weather Service, 2017]. Ground based technologies for atmospheric temperature measurements has not yet developed at the same rate as in other areas of atmospheric science and the industry is predominately dependent on radiosondes, satellites, and radiometers. There has been widespread expansion of lidar technology applications in topography mapping, mining industry, automated cars, forest inventory, and lately, camera resolution in phones and augmented reality, however, the exploration of commercial use of lidar in atmospheric temperature profiling is yet in progress.

Chapter 2.

Raman Lidar

2.1 Instruments and Technology

Lidar is the core technology used here for measurements of the vertical temperature profile of the atmosphere. The process involves emitting laser pulses at a frequency of 20 Hz from a lidar setup directed toward the sky through a roof opening, followed by the emitted light interacting with the atmospheric constituents in the path of the laser. The emitted light undergoes scattering from aerosols, cloud particles and gas molecules, and the resulting backscattered light is collected by a receiving telescope and detected using photon counting. The time between the laser pulse emitted by the source and received by the detector is used to determine height, which in this case is the vertical distance from the lidar system. The vertically resolved values of the received backscatter signal strength are used to produce a vertical profile of the characteristic of interest in the atmosphere. The lidar setup used in this analysis is built in an aircraft rack, shown in Figure 2.1, for easy installation on an airplane when needed, including during previously conducted airborne atmospheric ozone and aerosol measurements in Prof. Whiteway's research group.

Theoretically, the expected backscatter signal strength of a rotational Raman spectrum line at each height level, assuming hydrostatic equilibrium, can be calculated using Equation 1 below [*Behrendt*, 2005]

$$P_{RR}(z) = P_o \, \mathcal{E} \, \frac{A \, O(z)}{(z - z_o)^2} \, \Delta z \, N(z) \sum_i \sum_J \mathcal{T}_{RR}(J_i) \, \eta_i \left(\frac{d\sigma}{d\Omega}\right)^{RR,i} (J_i) \, \mathcal{T}_{atm}(z_o, z)^2 \quad (1)$$

where P_o is the strength of the transmitted signal, $\mathcal{E}$ is the detector efficiency, A is the free telescope area, $O(z)$ is the height-dependent overlap function between the laser beam and the telescope field of view, Δz is the height resolution, $N(z)$ is the air molecule density, $\tau_{RR}(J_i)$ is the transmission of the receiver at the RR wavelength line 'J_i', 'η_i' is the relative volume abundance of N_2 and O_2, and $\tau_{atm}(z_o, z)$ is the atmospheric round trip transmission. The differential term in Equation 1 is the pure rotational Raman differential backscatter coefficient, which is the ratio of the intensity of light energy scattered back in the direction of the detector to the incident energy. This term includes the Stokes and anti-Stokes contributions to Raman scattering. The overlap function and atmospheric transmission are described in Section 3.2.4. Only N_2 and O_2 are included in the molecular constituents because of its majority volume abundance in the atmosphere relative to other constituents.

The measurement and recording instrument setup at York University consists of a Nd:YAG laser transmitter, a receiver telescope consisting of an off-axis parabolic mirror, a blocking filter, a grating spectrometer, a 32-channel multispectral detector by Licel connected to a laptop with the Licel Windows software to record the measurements along with data acquisition electronics, shown in Figure 2.2. Nd: YAG (Neodymium Yttrium Aluminium Garnet) is a YAG crystal doped with Nd such that it replaces a small proportion of Yttrium ions in the crystal. It is the most common lasing medium used in commercial solid-state lasers today. The laser in the transmitter with 3rd harmonic generation emits pulses of electromagnetic radiation of 355 nm wavelength at a pulse energy of 80 mJ at a repetition frequency of 20 Hz. The laser light used for our measurements was linearly polarized. The light pulses are directed into the atmosphere by a reflecting mirror on a gimbal mount. The backscatter signal received at the detector setup is collected by an off-axis parabolic mirror telescope of diameter 15 cm, as shown in Figure 2.2. The field stop aperture at the focal plane of the telescope defines the conical field of view with a full angle of 1 mrad or less.

The received signal is then passed through an interference filter (edge filter) that blocks the elastic backscatter at 355 nm. An interference filter uses the properties of interference of light to discriminate between the different constituent wavelengths of the incident light. It consists of a coating of dielectric layers with spacing between the surfaces of the mirrors called the optical cavity of the filter. The incident light is reflected off the mirror's surface and this process is repeated multiple times in sequence to exploit even a small difference in the Fresnel reflection coefficient of the constituent wavelengths by multiple interferences. Interference is a function of the phase difference between the reflected wave and the incoming wave based on the path length travelled, creating constructive or destructive interference. Phase difference is given by '$k \times 2d \times n$', where '2d' is the distance travelled by the reflected wave in the cavity of length 'd', 'n' is the difference in the refractive index of the mirror and spacing, and '$k = 2\pi/\lambda$'. This results in the net reflection of the different constituent waves based on wavelength. The materials are selected to possess high reflectivity and close to zero absorption coefficient for the wavelengths of interest. The interference filter used in the instrument is an edge filter, which splits the incident light into parts- passbands and stopbands with the goal of minimizing transmittance of the stopbands and maximizing transmittance of the passbands. A long-wave pass (LWP) type edge filter was used which blocks wavelengths at 355 nm or shorter, and passes the longer rotational Raman wavelengths of interest for the analysis. The bandwidth of the filter is the range of the passed wavelengths, while a narrow range of wavelengths may lie on the edge of the filter which is the region in between the transmitted and blocked wavelengths. The width of this slope of transition between the two sections, which is an indicator of the performance of the filter, depends on the construction and design of the filter. A sharp slope is desired for optimizing the transmittance differentiation between the pass and blocked regions. This filter was beneficial in limiting elastic backscatter signal strength to focus on the rotational Raman

wavelengths, as seen in Figure 3.3, where the channel corresponding to elastic signal at 355 nm has smaller magnitude as compared to the channels detecting rotational Raman backscatter signal.

A fiber bundle takes the light from the telescope field stop to a grating spectrometer which disperses the wavelengths over a 32-channel photomultiplier detector. This detector is a new technology from Hammatsu Photonics and a complete system with 32 channels of photon counting data acquisition was provided by Licel GmbH. The spectrometer is set at a grating level of 0.347 nm/channel, centred at roughly 359 nm to establish a spectral range from 353.5 nm to 364.3 nm over the 32 channels of the detector.

Photomultiplier tubes (PMT) have been traditionally used for higher sensitivity in detection of low light levels in the UV, visible and near IR range. The photomultiplier tube is a linear multi-channel assembly of a photocathodes to a linear array of 32 dynode chains with a collection anode at the end of each channel that produces a photon-counting pulse for each photon incident on the photocathode. Each channel of the PMT consists of 3 main components- the photocathode, an arrangement of dynodes, and an anode in this order, as shown in Figure. 2.4. The photocathode is a photo-emissive surface in a vacuum that emits electrons when the incident photon energy exceeds its photoelectric work function, using the photoelectric effect. Each photon incident on the photocthode results in a photoelectron. The emitted electron is accelerated and focussed onto the first dynode where it is multiplied by means of secondary emission. This multiplication by secondary emission is repeated sequentially through a chain of dynodes in the tube. The trajectory of the emitted electrons is optimized for high collection efficiency and is determined by the design and construction of the PMT, which in the case of the Hamamatsu PMT used in our instrument setup was linearly-focussed. The multiplied, accelerated electrons emitted by the last dynode are finally collected by the anode at the end of the tube. The gain produced across the dynode chain is

determined by the selected voltage setting that accelerates the electrons and by the gain characteristics of the dynode. The collection anode outputs the electron current pulse to an external circuit.

The amplified and separated 32 raw signals are transmitted from the photomultiplier tube to the individual 32 discriminators of the Licel transient recorder (shown in Figure 2.3) and counters behind them, which count single photons for each channel individually. This way the Licel system discriminates, amplifies and counts signals of different wavelengths to provide 2-dimensional, spectral and range resolved data. The vertical resolution for measurements is controlled by setting the sampling bin length, which determines the resolution of the lidar data, and was set to 7.5 m for measurements used in this analysis. The total number of sequential range gated measurements per channel is 4000, which with the selected step-size corresponds to a vertical range of 30 km up from the height level of lidar at ground. The data acquisition software records the signal as photons counted per second. The data is transferred via Ethernet from the transient recorder to the connected laptop (with Windows Operating System) for storing the data.

The received backscatter induced photon counts are recorded for each channel over a user-selected number of shots or events set in the microcontroller of the counter, which was selected at 1200 shots (60 s at 20 Hz) for the data used in this analysis. Once the last shot in the set range of 1200 shots is received the photon-count value is saved digitally against the time of recording the first shot. This helps to interpret the signal more effectively with averaging that reduces the signal noise. The acquired, summed spectra over the vertical heights is viewed via the LabView software on the connected laptop. The operational specifications of the lidar system is outlined in Table 2.1.

Table 2.1: Specification table for the rotational Raman lidar system at York University.

Lidar system component	Specification
Transmitter	
Laser type	Nd: YAG
Laser wavelength	355 nm (3rd harmonic generator)
Laser energy	80 mJ/pulse
Laser pulse repetition frequency	20 Hz
Receiver	
Telescope type	Off-axis parabolic mirror
Telescope diameter	15 cm
Telescope Focal Length	50 cm
Telescope field of view	< 1 mrad
Spectrometer grating level	0.347 nm/channel
Photomultiplier tube	Hamamatsu 32-channel assembly
Detector	Licel 32-channel lidar detector
Spectral range over 32 detector channels	353.5 nm to 364.3 nm
Vertical resolution	7.5 m
Vertical range	30,000 km
Operating environment of detector	0º C to 30º C

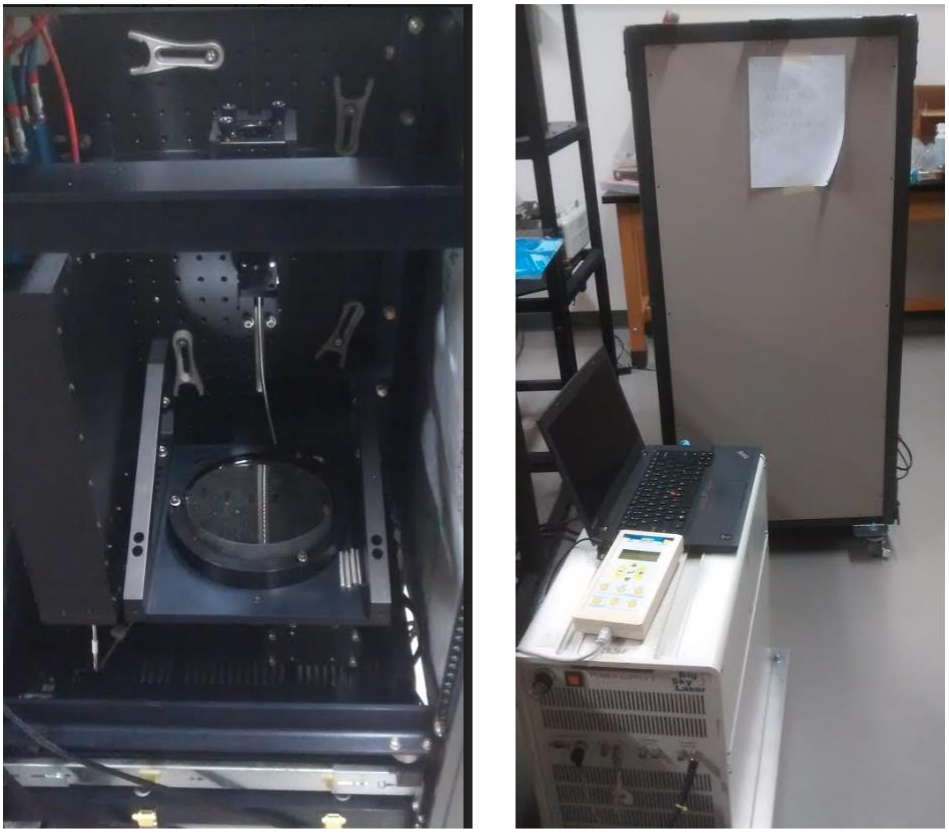

Figure 2.1. Photographs of the interior and exterior of the Lidar system at the York University laboratory.

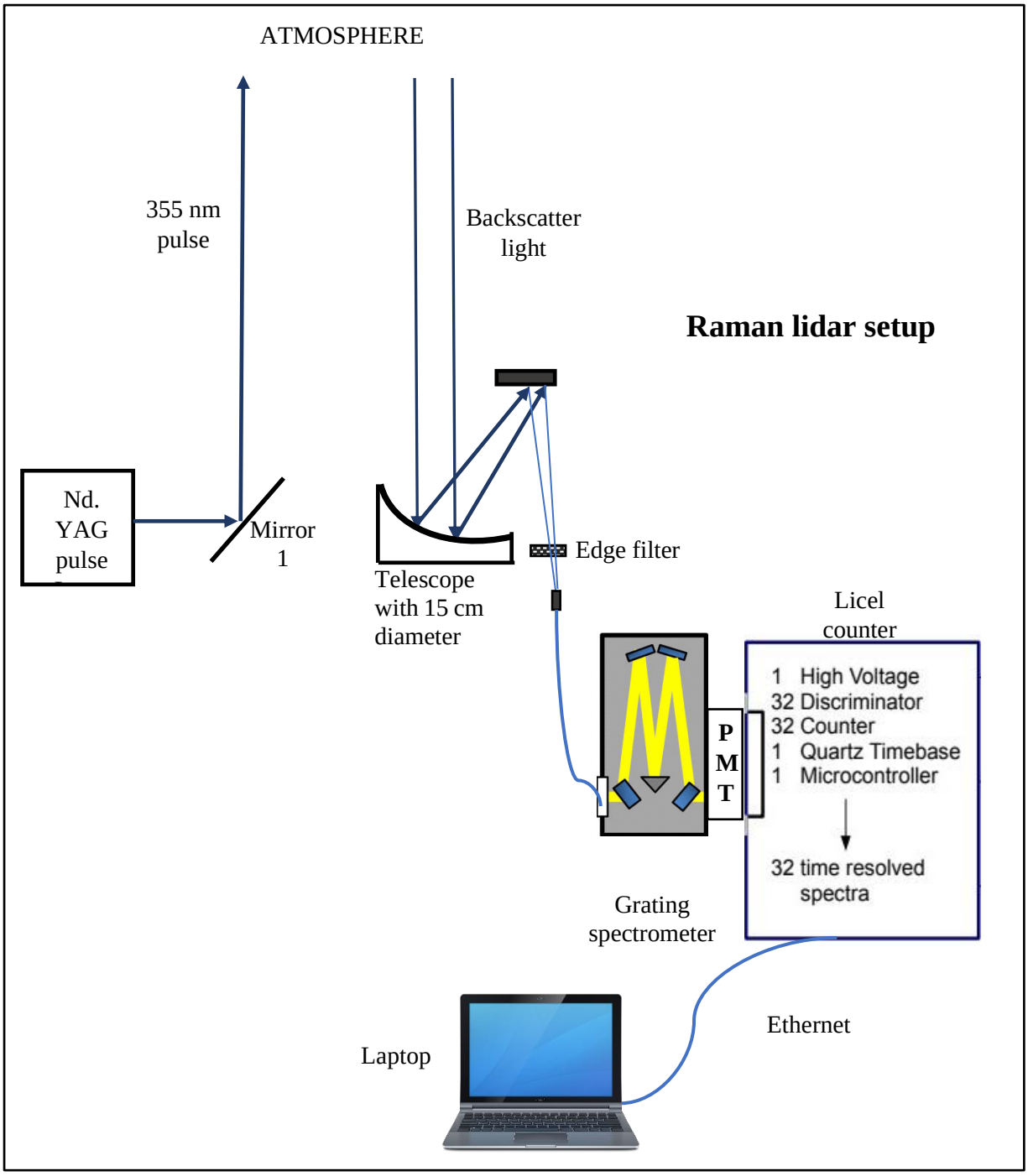

Figure 2.2. Diagrammatic scheme of the lidar system and Licel 32-channel multispectral detector at Prof. Whiteway's lab at York University.

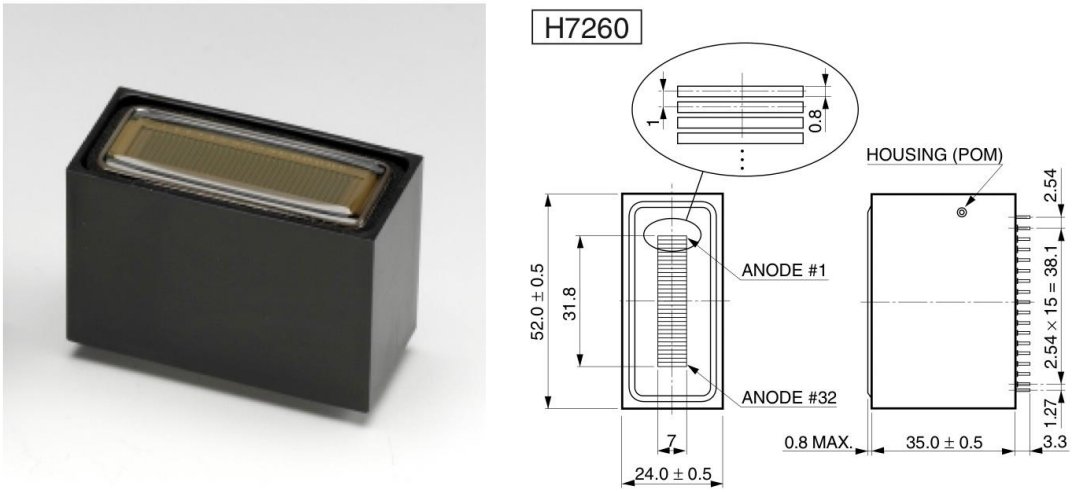

Figure 2.3. Licel multichannel detector is based on the Hamamatsu linear array multi-anode photomultiplier.

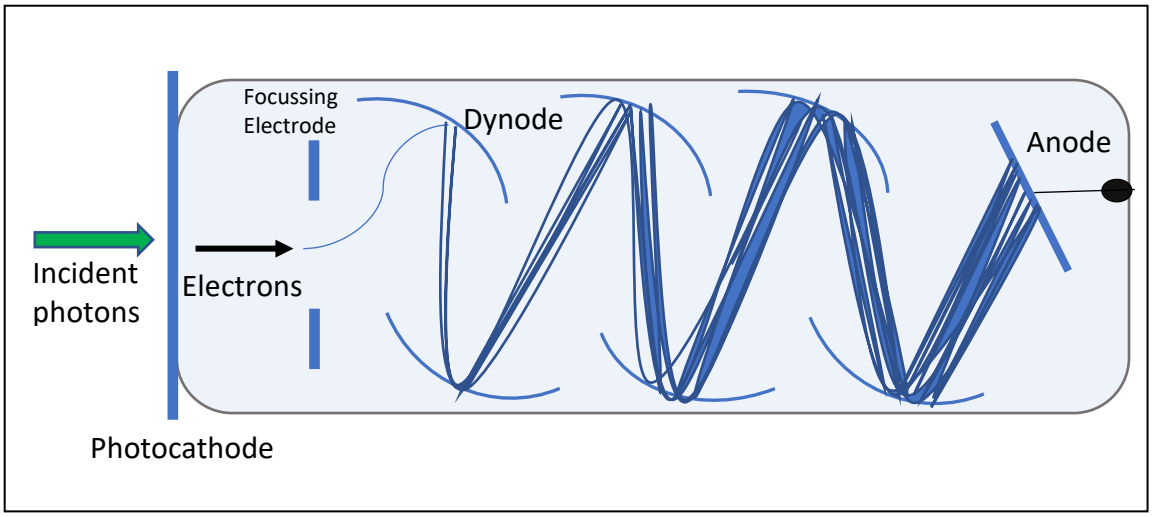

Figure 2.4. Diagrammatic representation of a single PMT channel with a photoelectric surface, dynode chain and collection anode. The Licel detector consists of 32 such channels for simultaneous detection of 32 wavelength-separated signals.

The Licel multispectral detector was a new addition to Prof. Whiteway's lab, replacing the earlier single-channel detector. Initial measurements using the new lidar system-multispectral detector for test runs were conducted starting February 2019. Lidar measurements of atmospheric backscatter signal used in this analysis were conducted in February, April and June in 2019.

2.2 Background and Theory

When a photon is incident on a molecule, it is absorbed and the energy gained results in the excitation of an electron in the molecule to a higher energy level followed by its subsequent fall to a stable, lower energy level. The energy difference in these two levels is emitted as a photon. If the electron falls back to the same ground state, there is no net transfer of energy to the molecule and the scattered photon has the same energy and wavelength ass ther incident photon. Scattering does not require the incident photon to match the energy gap between ground and a possible excited state. Rather, there is temporary polarization of the electron cloud of the molecule and it raising to a short-lived, higher 'virtual' energy state. This transition lasts about 10^{-14} seconds, with the molecule falling back to its ground state subsequently. The difference in the energy between these two states is emitted as a photon, which can be released in any direction, resulting in the scattering of light. The types of scattering explored in our analysis include Rayleigh and Raman scattering, while another major type is Mie scattering. The expected type of scattering to occur can be found by comparing the ratio of the radius of the particle and wavelength of light as '$x = \frac{2\pi r}{\lambda}$'. 'X' is close to 1 in the case of Mie scattering with the molecules having diameters larger or comparable to the wavelength of incident light. Rayleigh scattering occurs when particle size is much shorter, at least $1/10^{th}$ of the wavelength, so 'x' is significantly smaller than 1. In Rayleigh scattering, only the electron cloud of the molecule is distorted and the molecule falls back to the same ground state, so there is no energy loss or transfer of energy between the photon and molecule. The released photon has the same energy as the incident photon, so the wavelength associated with the photon remains the same, which is why it is called elastic scattering. The intensity of scattering by a molecule depends on the polarization of the incident light. For vertically polarized light used in our measurements, the scattered intensity

is independent of the direction of the scattering plane. Because of the spherical symmetry assumed for molecules, scattering patterns are symmetrical in three-dimensional space [*Liou,* 2002].

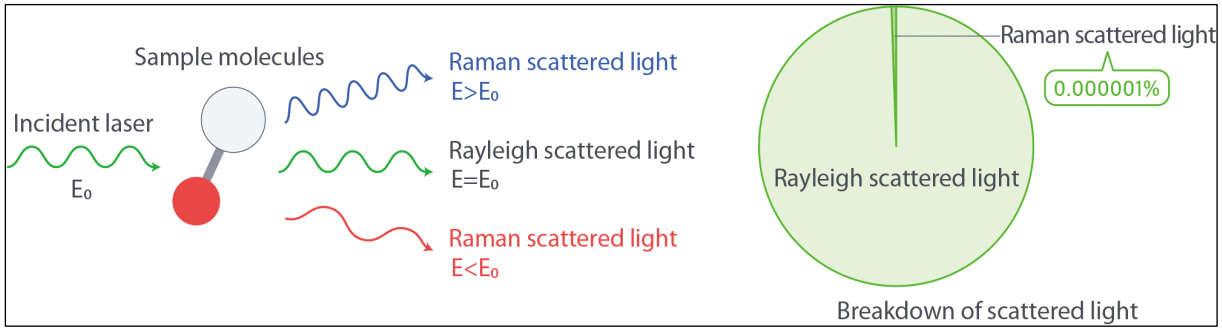

Figure 2.5. Raman scattering phenomenon explains the shift in wavelength in less than 1% of the total scattering by a given sample.

In polarizable molecules, the incident photon can excite vibrational modes within the electronic states of the molecule resulting in transitions in vibrational levels. If the molecule transitions to a vibrational state higher than the ground state, the difference in the levels is emitted as a photon with lower energy than the incident photon. This results in a shift to a longer wavelength and is called Stokes-shifted Raman scattering. If the molecule returns to a vibrational state lower than the initial state, the photon emitted has higher energy and a shift to a shorter wavelength relative to the incident photon, which is called Anti-Stokes shifted Raman scattering. Raman scattering can also occur with a simultaneous change in vibrational, rotational or electronic energy of the scattering particle. Transitions in rotational levels within a vibrational state of the molecule results in rotational Raman scattering. This occurs in molecules having anisotropic polarizability, that is, the polarizability depends on the molecule orientation which is the case in spherically asymmetric molecules. Non-polar molecules such as 0_2, N_2, and $C0_2$ exhibit rotational Raman spectra as well provided the molecules have an electric dipole moment, following the scattering of two energy levels and

transitions fulfilling the total angular momentum quantum number difference 'Δj' of ±2, explained further in this section. Generally, molecules undergo electronic transitions when excited by ultraviolet light, vibrational transitions when excited by infrared or visible light, and rotational transitions when excited by microwave or infrared light.

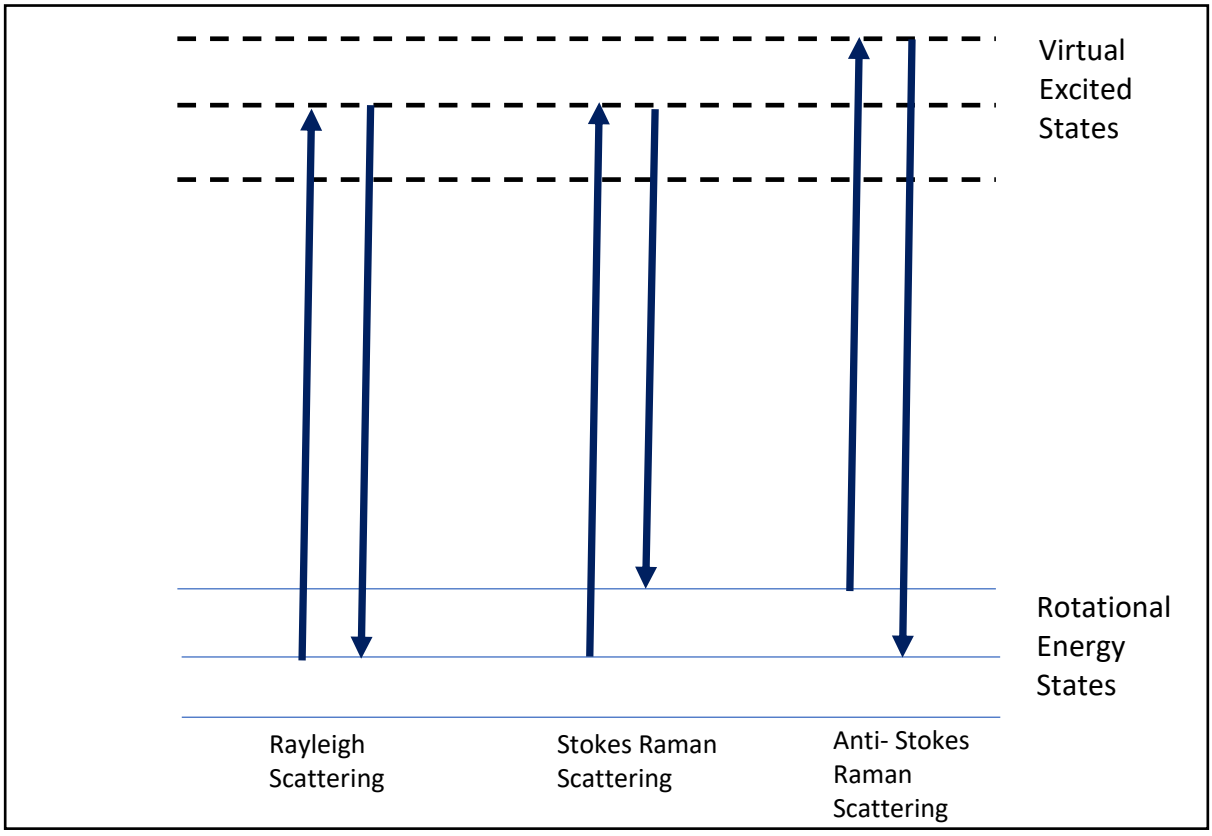

Figure 2.6. The vibrational transitions of a molecule in Rayleigh, Stokes Raman and anti-Stokes Raman scattering.

A photon incident on a molecule subjects it to the electric field associated with its electromagnetic radiation of given frequency ω_i. This field induces a small dipole moment in the molecule, given by:

$$\mu = \alpha E(t) = \alpha E_0 \cos(\omega_i t) \quad (2)$$

where ‘α’ is the polarizability of the molecule- a measure of the distortion of its electron distribution by an external electric field, ‘E_0’ is the amplitude of the electric field, and ‘ω_i’ is the frequency of the incident electromagnetic wave. If the molecule is rotating at an angular frequency of ‘ω_r’ and is anisotropic, then its polarizability will be time-dependent and can be represented as in Equation 3 [*Kampfrath et al*., 2018].

$$\alpha(t) = \alpha_o + \Delta\alpha \cos(2\omega_r t) \tag{3}$$

where α_o is the average polarizability from perpendicular and parallel components, and $\Delta\alpha$ is the anisotropic polarizability component resulting from the difference in the perpendicular and parallel contributions depending on the orientation of the molecule relative to inducing electric field.

$$\alpha_o = \frac{2\alpha_\perp + \alpha_\parallel}{3} \tag{4}$$

$$\Delta\alpha = \alpha_\parallel - \alpha_\perp \tag{5}$$

The total polarizability of an anisotropic molecule, α varies from $\alpha_o + \Delta\alpha$ to $\alpha_o - \Delta\alpha$ as the molecule rotates from 0º to 360º, respectively. Substituting the above polarizability equations in Equation 2 to give the total induced moment gives below equation.

$$\mu = \alpha_o E_0 \cos(\omega_i t) + \frac{1}{2} E \Delta\alpha [\cos(\omega_i + 2\omega_r)t + \cos(\omega_i - 2w_r)t] \tag{6}$$

The first term of the above equation represents the oscillations at the same frequency as incident radiation ω_i, so the transitions resulting from this component represent Rayleigh scattering with the frequency of the emitted photon remaining the same as the incident frequency. The second term represents rotational Raman scattering and requires anisotropy, that is, $\Delta\alpha$ should not be 0. The term accounting for frequency higher than the incident radiation $\omega_i + 2\omega_r$ represents Anti-Stokes scattering in which the emitted photon has higher

energy, while the term corresponding to lower frequency $\omega_i + 2\omega_r$ represents Stokes scattering with the emitted photon having lower energy than the incident photon. Since rotational Raman scattering involves two photons, each with spin 's' = 1, the transitions allowed in this type of scattering correspond to a change of ± 2 in the total angular moment quantum number 'j'.

In conclusion, the rotational Raman backscatter process involves a shift in frequency of electromagnetic radiation to lower or higher values relative to the incident frequency, corresponding to Stokes and Anti-Stokes spectrum lines, as seen in Figure 2.7. The distribution of individual line intensities associated with transitions of rotational states in molecules depends on the temperature of the system. The shift in wavelength in the backscatter signal corresponds to a shift in the scattering particle's characteristic vibrational and rotational energy, which can further be represented as a function of temperature to identify and construct a temperature-dependent relationship of the received backscattered Raman light. This temperature-dependency is leveraged in this thesis to determine the vertical temperature profile of the atmosphere. Raman scattering effect is the main phenomenon based on which this analysis was conducted.

Rayleigh scattering accounts for more than 99% of the total scattering undergone by light, while Raman scattering constitutes the remaining less than 1% of the total scattered light, as shown in Figure 2.5. Only 1 in 10^6 to 10^8 of the incident photons is Raman scattered, so the strength of the received Raman backscatter signal is even lower than the Rayleigh signal and many times lower than that of the emitted laser pulse. This is why a blocking interference filter was used to restrict the elastic signal at 355 nm .

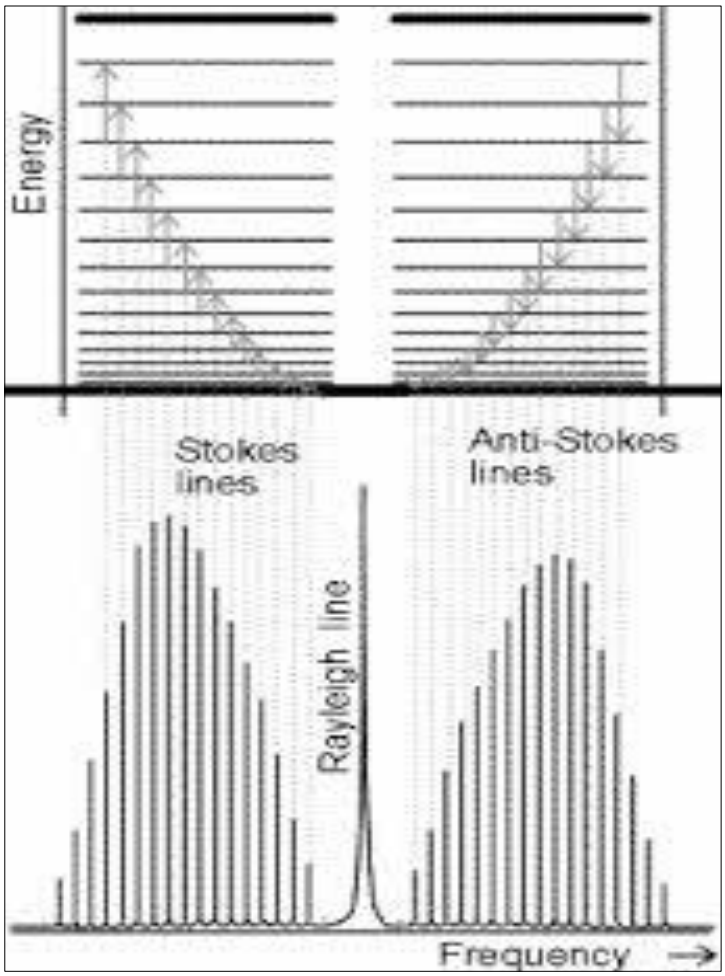

Figure 2.7. Stokes and Anti-Stokes lines in Rotational Raman Scattering with corresponding Raman spectrum [DCU School of Physics Sciences, 2020].

To develop an atmospheric temperature profile using rotational Raman scattering measurements, the ratio of the backscatter photon-counting signal of two pure rotational Raman lines, S_{RR1} and S_{RR2}, is taken [*Di Girolamo et al.*, 2004].

$$Q\,(T,z) = \frac{S_{RR2}(T,z)}{S_{RR1}(T,z)} \tag{7}$$

Ideally, the two selected rotational Raman spectra lines should have opposite temperature dependence. A linear combination of two or more signals can also be taken to establish the temperature dependence. The direct correlation of the ratio of rotational Raman backscatter signal and temperature is given by substituting Equation 1 in Equation 7, with

components of the equation cancelling out since the transmitted photons, detector efficiency, telescope area are the same throughout the span of measurements, given no changes are made to the lidar settings and hardware. The ratio of the rotational Raman lines is taken at the same height levels, so the molecular number density function, overlap function and atmospheric round-trip transmission cancel out since these are a function of height only and these values would be same assuming the atmosphere is in a hydrostatic equilibrium. So, the ratio simplifies and can be represented as a function of temperature only, given by Equation 8 [*Behrendt*, 2004].

$$Q(T) = \frac{\sum_{Ji} \tau_{RR2}(Ji) \left(\frac{d\sigma}{d\Omega}\right)^{RR,i}(J_i)}{\sum_{Ji} \tau_{RR1}(Ji) \left(\frac{d\sigma}{d\Omega}\right)^{RR,i}(J_i)} \quad (8)$$

One way to solve for temperature-dependence of the ratio *Q(T)* in Equation 8 is to calculate the differential backscatter cross-section area $\left(\frac{d\sigma}{d\Omega}\right)$ for atmospheric molecules, predominantly 0_2 and N_2, for the two selected Raman wavelengths and input the transmission values of the lidar at the wavelengths of the rotational Raman line J_i. Another way is to simply calibrate the ratio of the backscatter signal received at two Raman wavelengths with vertical atmospheric temperature using measurements from a support source, such as a nearby local radiosonde or weather station. Once the calibration function has been identified and confirmed using a set of measurements, the function should hold true for all lidar measurements conducted with the same settings even on different days. The calibration of the signal ratio dependency on temperature can be optimized by including either just the ratio of two Raman signals or the ratio of a linear combination of multiple Raman signals. Using this calibration of signal measurements, the signal ratio can be related to temperature as below [*Di Girolamo et al.,* 2004].

$$Q(T) = e^{\frac{a}{T}+b} \quad (9)$$

In Equation 9, a and b are calibration coefficients. This equation can be modified to a quadratic or cubic function of temperature if needed to optimize the fit to the measurement data, as performed in this analysis and explained in Section 4.

Chapter 3.

Measurements and Analysis

3.1 Lidar Measurements

Lidar measurements were conducted at our laboratory at the Petrie Science and Engineering building at York University at night-time to limit the background, extraneous light from solar radiation and ideally in clear atmospheric conditions to minimize the noise in the signal. Figure 3.1 shows the difference in daytime and night-time recorded measurements on the same day, with the daytime Raman backscatter lidar signal consisting of larger background light from solar radiation. This causes the daytime Raman signal to have higher signal uncertainty relative to signal strength throughout the vertical profile and overall larger signal uncertainty at higher heights compared to night-time measurements. Therefore, night-time measurements of backscatter Raman signal were used in this analysis. Greater background signal during measurements would increase the statistical variance in the background recorded in each range bin. Although the background could be subtracted from recorded signal, the large statistical variance could not. This noise is the main factor in limiting the maximum height for measurements. Correction for the contribution of the background light in the backscatter signal is explained in Section 3.4.1.

The presence of clouds is clearly observed in the backscatter signal profile by sudden, sharp increases in the elastic backscatter signal profile, as observed during evening measurements on February 21, 2019 shown in Figure 3.2. The higher aerosol concentration in the cloud layers contributes to larger scattering of the elastic laser pulse. The elastic

backscatter signal is strong enough that measurements of cloud and aerosols can be carried out in daytime as well. If lidar measurements are performed in cloudy conditions, it is important to check for any increase in the rotational Raman signal at the cloud altitudes due to leakage of the elastic backscatter signal in the Raman channels. All the data analysis for lidar signal measurements and relating calculations were performed using MATLAB.

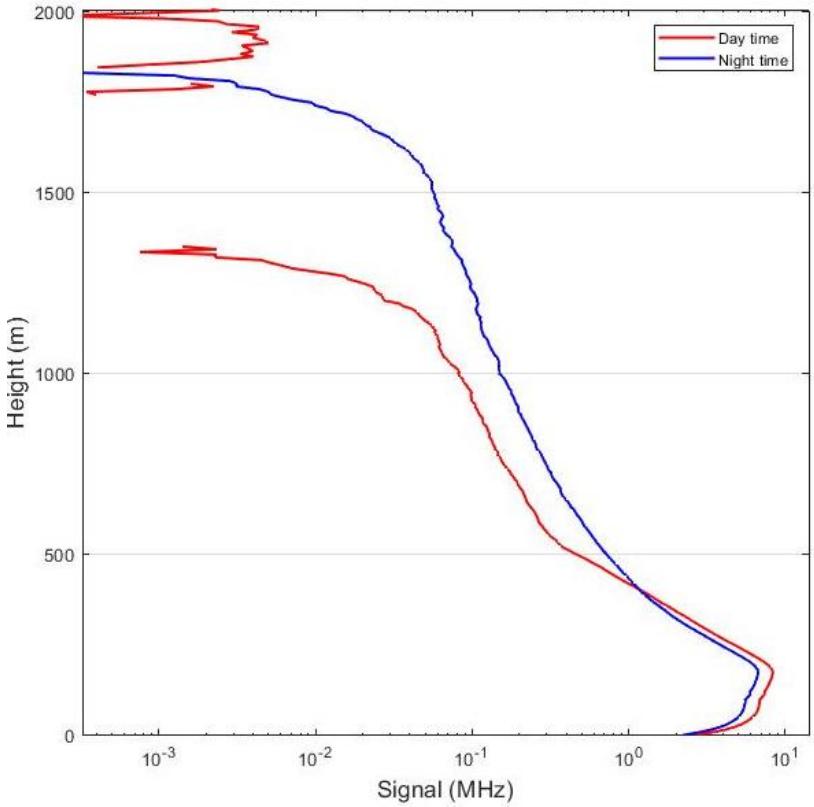

Figure 3.1. Comparison of background-subtracted backscatter lidar signal at the rotational Raman wavelength at 356 nm between night and daytime measurements on April 16, 2019 at York University. The daytime Raman signal has higher contribution from background, as reflected in the figure by the gap in the day-time signal profile after background subtraction.

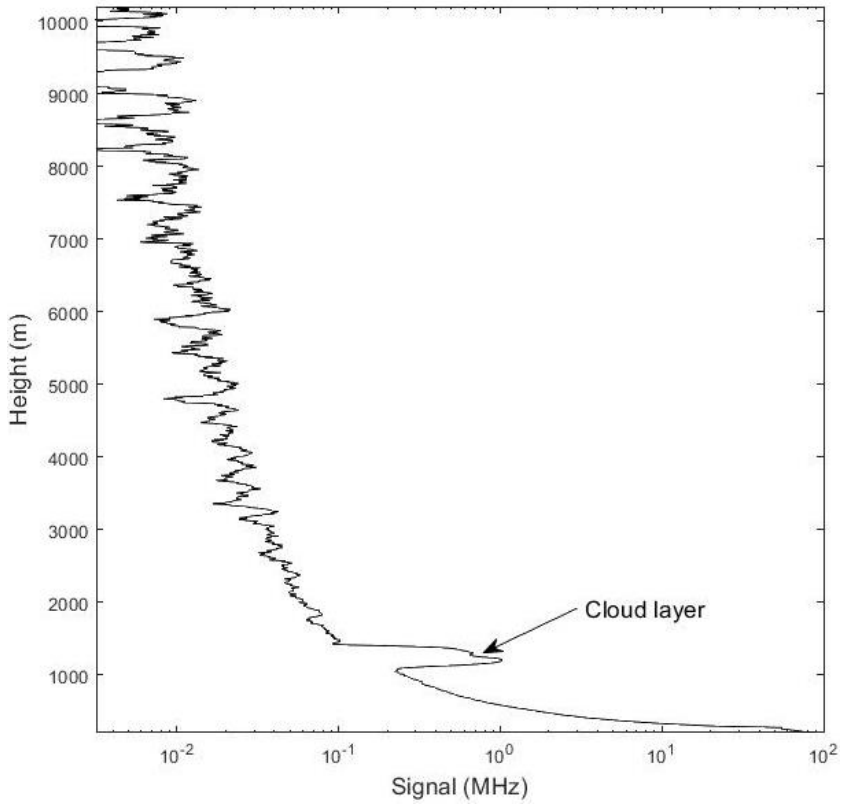

Figure 3.2. Elastic backscatter signal recorded from lidar measurements on February 21, 2019 at York University with visible cloud layer at around 1200 m.

Lidar measurements for temperature profiling were conducted in winter on February 19, February 21, April 18 and April 30, and in summer on June 6, June 11 and June 12 in 2019. A minimum of two sets of measurements are needed to generate a temperature profile: one set to calibrate the rotational Raman signal ratio measurements to local, vertically-resolved atmospheric temperature values, and the second set to apply the calibration function to produce a temperature profile and check for accuracy by comparison with local measurements from other sources. Rotational Raman measurements conducted between 6:35 pm to 7:27 pm on April 18, 7:03 pm to 9:29 pm on April 30, 7:41 pm to 10:49 pm on June 6, 7:50 pm to 11:00 pm on June 11, and 6:50 pm to 11:28 pm on June 12 in 2019 were used in this analysis. The total received backscatter signal data had three dimensions- time value, height value and wavelength value. The backscatter signal recorded at each of the 32

channels of the detector, corresponding to a range of 32 wavelengths, were averaged over the total duration of measurements on each day to limit the noise and anomaly events occurring at instances in the measurement duration, which made the data two-dimensional. The step value is the incremental vertical value of measurements which is converted to height in meters by multiplying with the step-size or vertical resolution, which was 7.5 m for the measurements in this analysis.

3.2. Selecting Raman Wavelengths

At the set grating level of the spectrometer, a spectral width of 0.347 nm is recorded between the centre of one channel and the adjacent channel. Each channel has a width of 0.8 mm over which a 0.2776 nm-wide spectra is recorded. The rotational Raman backscatter signal recorded at each channel is a result of the rotational transitions in all molecules contributing to scattering at the shifted wavelength, given by the summation sign in Equation 8. Therefore, the backscatter signal at each channel results from multiple rotational spectral lines within the 0.2776 nm spectral range of one channel.

To generate a temperature profile using the lidar signals, the ratio of two rotational Raman wavelengths is required, as given by Equation 7. There were six wavelengths sampled within the rotational Raman scattering spectrum, indicated as circular points in the Raman scattering region between channel 22 and 27 in Figure 3.3, corresponding to a spectral range of 355.3 nm to 357 nm. The two wavelengths at the wings of the spectrum at channel 22 and channel 27 were not used since the signals here were relatively small. The backscatter signal from the remaining channels were plotted against height and compared on signal strength and trend-dependence on height. The channel signals with a stronger trend or correlation with height would have a stronger sensitivity to temperature since temperature decreases mostly

consistently with altitude by the lapse rate for a given location and season. The lapse rate depends strongly on atmospheric humidity and is generally higher in drier, northern latitudes, around 8-9º C per km [*Hurell and Meehl,* 2006]. Therefore, the Raman signal having a strong, consistent trend with height is selected since it would be a stronger function of temperature. This would optimize the temperature dependency of signal ratio and reduce the statistical error in applying the calibration function of one day to signal recorded on other days. The calibration was further optimized by evaluating all combinations for the ratio of linear functions of Raman signals at the four feasible wavelengths assessed.

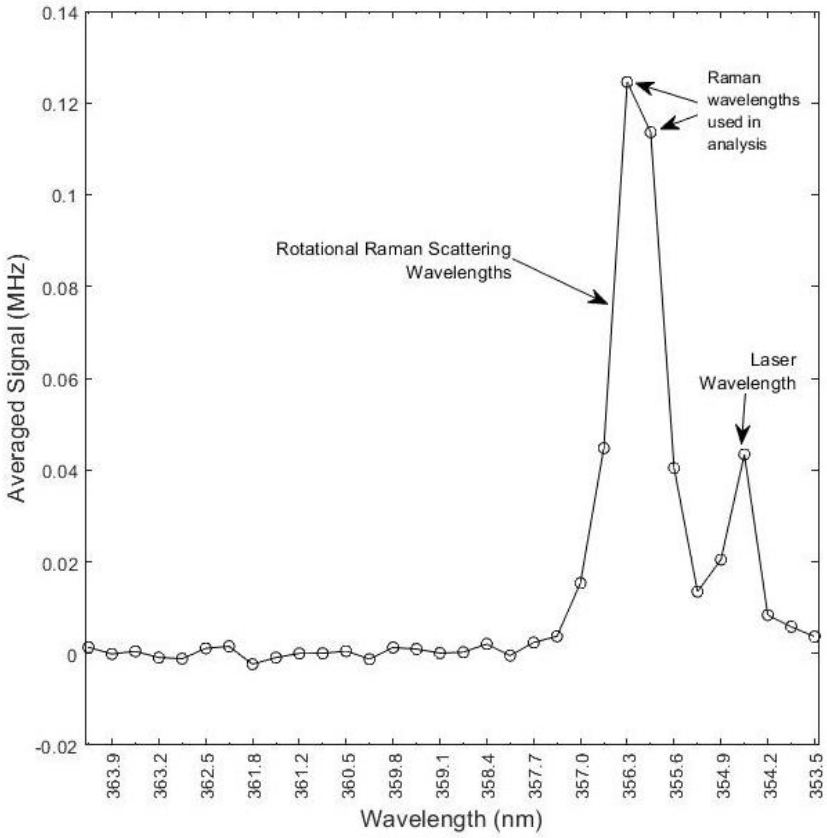

Figure 3.3. Spectrum of averaged Raman backscatter signal in the 32-channels of the Licel detector corresponding to a range of wavelengths from 364.3 nm to 353.5 nm, measured on June 6, 2019.

The channels producing a ratio with significant signal strength in the height range of interest and with a strong vertical trend were channels 24 and 25, corresponding to

wavelengths 356.3 nm and 356 nm, respectively. Figure 3.3 shows the backscatter Raman signal averaged for all heights across the 32 channels of the detector.

3.3. Error Analysis and Propagation

The statistical uncertainty in the signal measured with the lidar system is due to the variance in the detected photons. The signal is recorded in photon counting mode using the PMT. An integration period of 1200 shots was used to measure each backscatter signal value to reduce the statistical uncertainty in the signal. The photons incident on the photocathode of the PMT during any time interval is fundamentally uncertain even if the radiation incident has a constant intensity. The number of photons arriving per unit time are discrete and random events, with the probability of one event independent of others. The average time between events is known from multiple observations, that is, the recorded photon-counting signal over a certain observation period. Fulfilling these conditions, the rate of arrival of photons follows a Poisson distribution [*Liu et al.,* 2006]. In the PMT channels, the ejection of electrons from the photocathode for each corresponding photon also follows Poisson distribution and it is this statistical variance that contributes to the uncertainty in the measured signal. The standard deviation for a Poisson process is calculated as [*Bevington and Robinson,* 1993]

$$\sigma = \sqrt{\mu} \tag{10}$$

$$\mu = \frac{\text{signal}_{PC} \text{ x } r_z \text{ x } 1200 \text{ x } n}{c} \tag{11}$$

where 'μ' is the mean number of photon-counts recorded in the signal and '$signal_{PC}$' is the signal measured in photon-counting rate. The signal was recorded with a 7.5 m vertical bin width setting *(r_z)*, therefore, the number of photons in each range interval is *$signal_{PC}$ x*

r_z/c, where c is the speed of light. Each data file is averaged over 1200 laser shots and the compiled backscatter data for each set of measurements is averaged over the number of measurement files recorded in that set, n. This temporal averaging is accounted in Equation 10 as $1200 \times n$. The vertical smoothening of the raw backscatter data using a moving mean of 150 m is also accounted for in the error calculation. Using Equation 10, the statistical uncertainty in the lidar signal for all detector wavelengths was calculated, as shown for Raman wavelength at 356 nm in Figure 3.4. It is observed that the Raman signal above a height of 1500 m has large signal noise relative to the signal strength. Analyses in this thesis using Raman signal data were performed up to a maximum height of 1500 m.

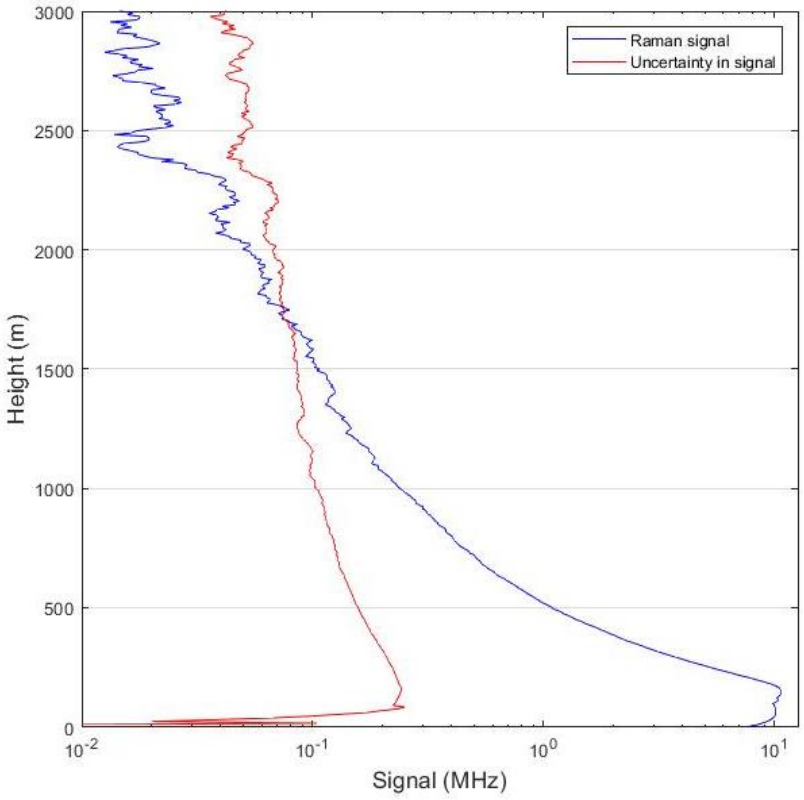

Figure 3.4. Lidar signal recorded at Raman wavelength of 356 nm and the calculated statistical uncertainty in the recorded signal for measurements on June 6, 2019 at York University.

The calculated error in the signal data was propagated for subsequent calculations of signal ratio and temperature, given by Equation 27 and explained in Section 4.3. The standard

calculations of multiplication, division, logarithmic and square root of values with error were used in propagation of error. The uncertainty in the lidar signal-derived temperature is shown using error bars in the derived temperature profiles in Section 4.4. The uncertainty in the calculated temperature increases with altitude since the uncertainty in the photon-count signal relative to the signal strength also increases with height.

3.4. Corrections

3.4.1. Background Correction

The background is the constant signal in recorded measurements. This background light is due to skylight and is contributed to from natural sources such as solar radiation, moonlight and star light, as well as city lights and traffic. The photon-count signal above 20 km, which is the signal data recorded in the last 1333 bins of lidar measurements, was averaged for each individual channel and subtracted from the signal received at all heights to correct for the background photons present in the Raman and elastic backscatter signal. The signal received from elastic scattering at the laser wavelength of 355 nm is recorded at channel 29 of the detector. The backscatter elastic signal is from molecules and aerosol, whereas the rotational Raman signal is only due to scattering from molecules. The signal strength of a detected Raman wavelength with and without background subtraction is shown in Figure 3.5. Background contribution adds to uncertainty in the measured backscatter signal. The background-corrected signal for the elastic wavelength and two Raman wavelengths used in the analysis is shown in Figure 3.8.

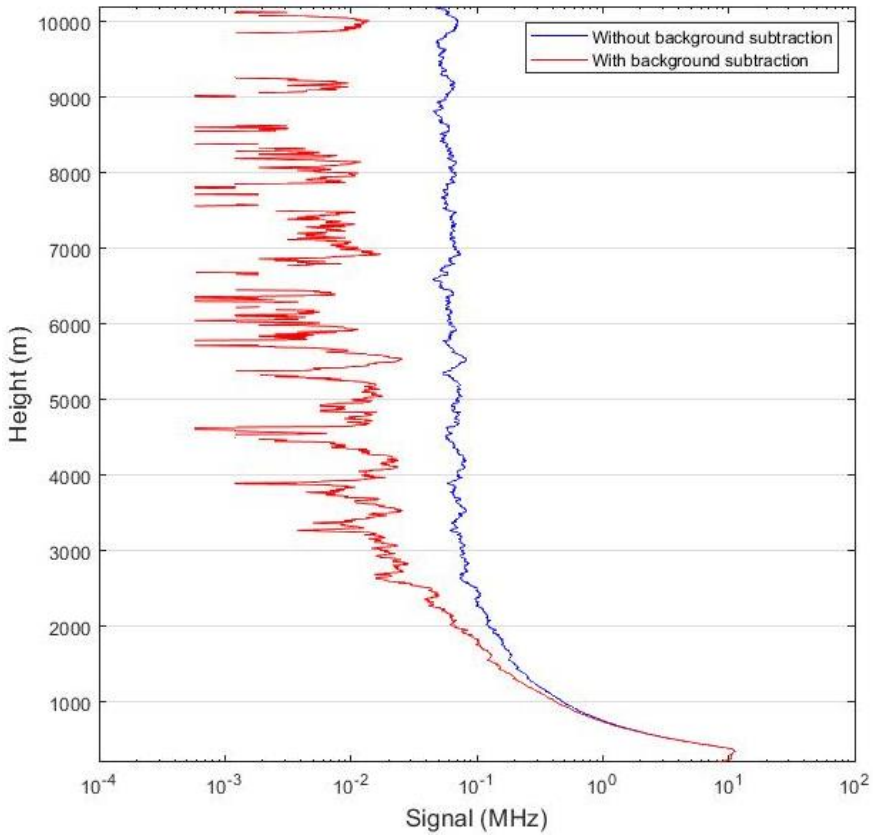

Figure 3.5. Measured Raman backscatter signal strength at 356 nm with and without background subtraction from lidar measurements on June 6, 2019.

3.4.2 Pulse Overlap in Photon-Counting and Non-Linearity Correction

To obtain accurate information about atmospheric characteristics, recording of the backscatter signal must have high sensitivity for all vertical ranges, especially at higher altitudes at which the backscatter signal strength is low. The lidar signal is detected in photon-counting mode which is highly sensitive for low level signals. The sensitivity of the detector to the light incident on the photocathode is given by the quantum detection efficiency or cathode radiant sensitivity, which is the probability of an incident photon to trigger ejection of one photoelectron at the photocathode. This detection efficiency varies over a broad range of wavelengths but is mostly constant for a shorter spectral range, including the complete 10.757 nm wavelength range over the 32 channels in the detector. This should result in a consistently linear proportion of the number of photoelectrons emitted

by the cathode to the number of photons incident on its surface. However, the system dead-time can cause inconsistencies between the optical signal and recorded photon counting signal. Dead time of the system, 'τ' is the recovery time required by the system after registering a photon before being able to register the next one, and it is an inherent characteristic of the instrument. It is the minimum time required by the system in between sequential photon detections, within which the system is frozen or unable to record. In general, there are two types of systems for which a dead-time correction of photon counting data is applicable: paralyzable and non-paralyzable systems. In paralyzable systems, subsequent events that arrive within the dead-time period restart the dead-time duration of the system from the time of the second event's arrival and extend it by another period 'τ'. This causes a prolongation of the period during which the events subsequent to the first are not registered. The Licel detector system is non-paralyzable and the events arriving within the dead time are simply lost and not recorded, and do not cause a further extension in dead time. Therefore, future events of incident photons are impacted linearly and consistently as the dead time value remains the same at 2.4 ns.

As the received signal level increases, the response of the PMT detector becomes nonlinear because of the pulse pileup effect. This is caused when the time interval between two incident photons at the photocathode is short enough, so the corresponding output pulses of the photomultiplier tube will overlap with each other and cannot be distinguished by the discriminator limited by its resolving time [*Donovan et al.,* 1993]. A large dead-time of the detector also increases the probability of a pulse pile-up [*Lee et al.,* 2020]. If the repetition rate of the overlapping output pulses is high, a significant loss in signal detection may be caused which would increase the disproportion of the output signal to the actual signal by a large factor. This nonlinearity in photon-counting influences the output signal in high rates of incident photons, which is the case in the backscatter signal from near-ground levels or any

prominent scattering material in the path. This causes the recorded signal strength to be lower than expected and the accuracy of photon-counting rate is limited to weak signals.

To correct for this nonlinearity and to increase the range of accurate photon-counting detection by the system, two sets of lidar signal measurements- with and without an attenuating, neutral density filter were performed. The filter used had a transmission factor of 1/6, so the detector recorded $1/6^{th}$ of the incident signal strength. Since the non-linearity in photon-counting arises in high signal strengths, using the transmission filter maintains the signal strength would be below the range of non-linearity. Multiplying the detected signal with the inverse of the transmission factor (i.e. 6) gives the true incident backscatter signal value. The ratio of the attenuated signal multiplied by the transmission factor of the filter to give the true signal strength and the unattenuated signal should ideally be unity across all signal ranges in the case of perfect linearity in signal counts. However, for higher signal counts in the case without the transmission filter, the dead-time influenced pulse-pileup causes non-linearity and the recorded signal counts are lower than the actual strength. This causes the ratio of the attenuated to unattenuated signal to decrease below 1. One way to correct this and increase the extent of linearity of this ratio is by deriving the true photon-signal count by accounting for the dead time in calculating the true signal as below.

$$\text{true signal} = \frac{\text{measured signal}}{1 - (\text{measured signal} * \text{dead time})} \tag{12}$$

Although the detector is expected to have an inherent dead-time of 2.4 ns as per the Licel system documentation, values within ± 0.1-0.5 ns of 2.4 ns were evaluated for possible dead-time to optimize correction for non-linearity in signal count using Equation 9. The most efficient correction for expanding linearity in higher signal counts was found using a dead-time value of 2.5 ns which extended linearity to up to 100 MHz counting rate. This was found by plotting the ratio of the non-linearity corrected signal measured without the filter and the

signal measured with the filter multiplied by the transmission factor. This ratio was plotted against a range of signal strengths for different dead-time values to identify the case for maximum extension of linearity, as shown in Figure 3.6. Further, this linearity ratio for channel 25 was divided with the linearity ratio of channel 24 respectively to give a value expected to be 1 in the case the ratio of linearity for the signal ratio is perfect linear. This divided value is plotted against the true measured signal (actual signal strengths) for both channels to check for linearity in channel ratio for all possible received signal strengths, as shown in Figure 3.7. This confirms that using Equation 10 to correct for nonlinearity in all channel signals would be effective for up to 100 MHz, which is the highest detected rotational Raman signal strength from lidar measurements.

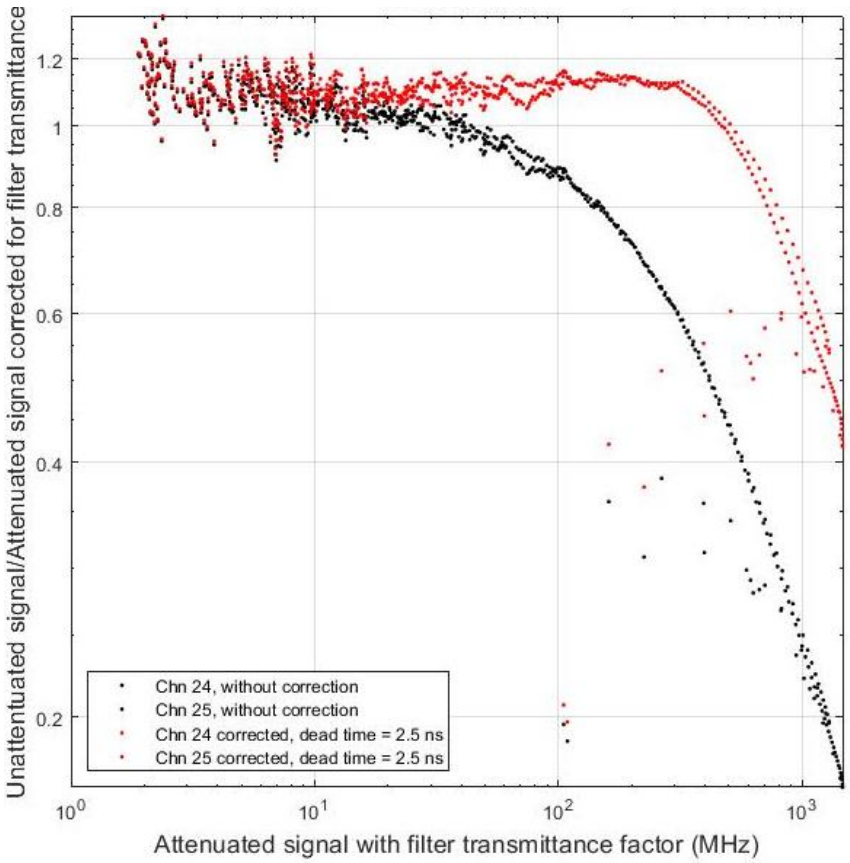

Figure 3.6. Nonlinearity correction for the detector dead-time of 2.5 ns increases the linearity in received photon-counts to signal for higher signal levels of upto 100 MHz in channel 24 and 25 used in this analysis.

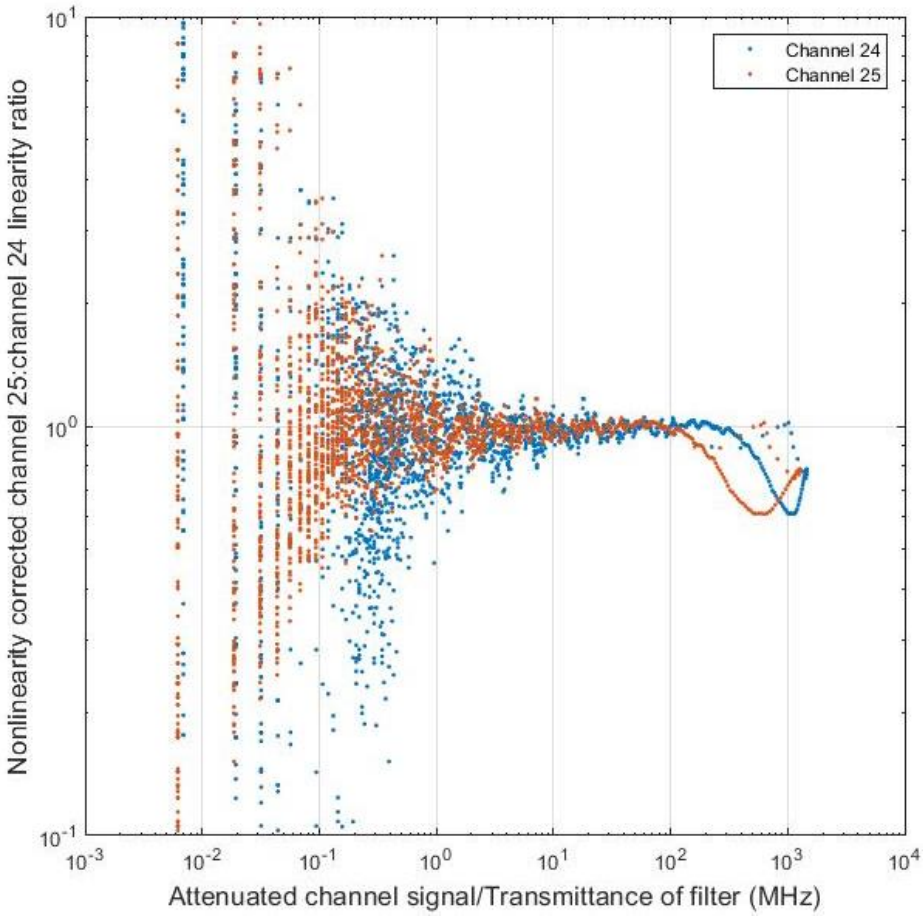

Figure 3.7. Correction for nonlinearity helps increase the linearity ratio for the ratio of signal in channel 25 to channel 24 to 1 for signal strengh of up to 100 MHz, which is within the magnitude of the maximum signal measured in this analysis.

3.4.3 Cross-talk between Detector Channels

The Licel system has two effects contributing to signal leakage between adjacent channels in the detector. One is the presence of stray light from the grating spectrometer that contributes to backscatter signal from wavelengths other than the monochromatic wavelength corresponding to that particular channel, and second is the signal leakage or the cross-talk between adjacent channels. The typical stray light levels in the detector are of the order of 10^{-4} MHz, which is very small relative to the signal strength in the height ranges used in the analysis, which is of the order of 10 to 10^{-1} MHz from ground to around 2 km up for the rotational Raman measurements. Cross-talk is the signal leakage which occurs between

channels when photoelectrons are emitted toward the dynode chain of the neighbouring channel, resulting in these photons being detected in the unintended channel. The signal leakage in neighbouring channels in the Licel detector ranges from 3% for adjacent channels, 0.6% for n+2 channels and 0.1% for n+3 channels on either side. This is corrected in each channel individually by subtracting the respective leakage percentage of other channels from the total signal recorded in the channel.

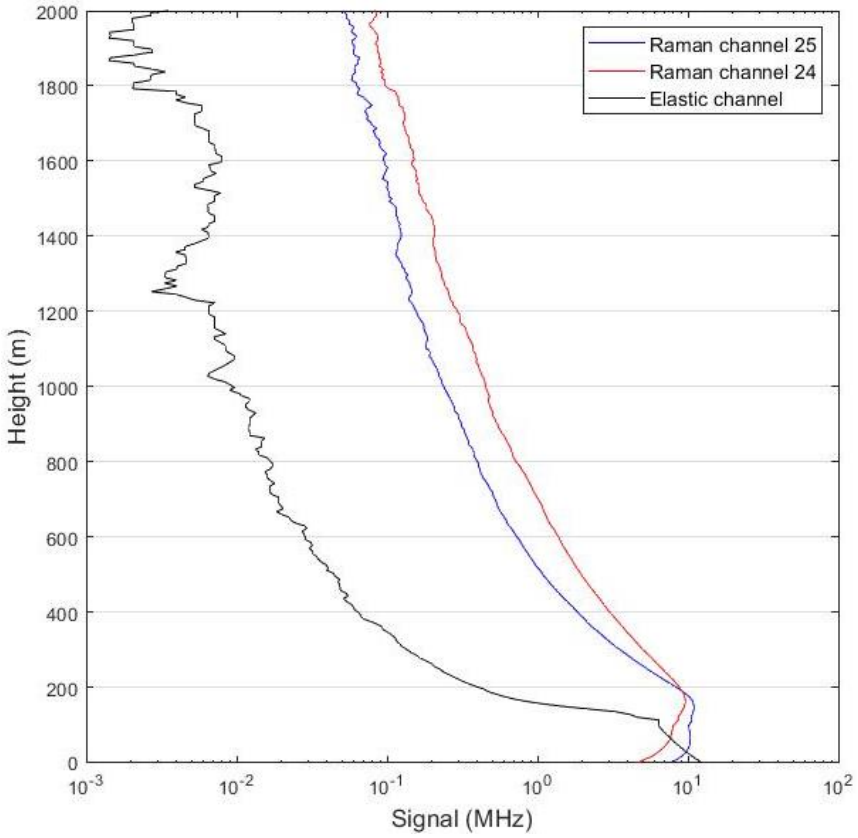

Figure 3.8. Background-subtracted, photon-count nonlinearity corrected and channel cross-talk corrected lidar backscatter signal for Raman and elastic wavelengths on June 6th, 2019 at York University.

3.4.4 Temperature Dependence of the Edge Filter

The working and function of the long-wave pass type edge filter used in the lidar setup is described in Section 2. The filter is susceptible to a shift of the wavelengths lying on the

edge of the filter with a change in temperature, which impacts the transmission of wavelengths analysed between different days under varying temperature conditions. This inherent susceptibility, if any, of the filter and the degree of wavelength displacement is unknown for the filter used and was analysed to account for the change in transmission of the filter on different days for optimizing the application of the calibration function. Since the Raman wavelengths used in the derivation of the atmospheric temperature profile lie on the edge of the filter, any shifting of the edge of the filter is expected to have a large effect on the transmittance of those Raman wavelengths. Characteristics such as the paired optical properties of the multilayers, the refractive index of the constituent materials which effects the index contrast of the cavity and the mirror, and the physical thickness of the materials have inherent temperature dependency [*Rohr and Hawkins*, 2015]. Temperature has an effect on the resistivity and thickness of materials, and this effect is especially substantial in thin films. Materials which expand the thickness of layers with an increase in temperature have a positive temperature coefficient, which is the case for most paired materials. The filters are constructed in cold and temperature-stabilized conditions, whereas the operating conditions for most instruments is warmer and uncontrolled including the working environment of our lidar instrument setup for the atmospheric Raman backscatter measurements. While the laboratory room temperature varies depending on the air-conditioning and heating that is controlled for the building, the added exposure to outside temperature conditions because of the opening in the laboratory roof to send and receive light signals from the atmosphere increased the variance in the room temperature greatly. Measurements were conducted in peak summer in June and in winter in February and April. An increase in temperature leads to optically thicker coating layers of the filter for materials, which causes a shift of the wavelengths on the edge toward longer wavelengths. Since the backscatter signal is detected by channel numbers of the spectrometer which correspond to specific, unique wavelength

numbers determined by the grating set for the measurements, the shift of the edge causes a change in the transmittance function of wavelengths. This effects the magnitude of the signal detected for a wavelength and the ratio of the signal at two wavelengths, which is directly used in this analysis for the temperature derivation. Theoretically, the shift of the wavelengths on the edge of the filter with temperature change can be described by below equations. [*Rohr and Hawkins*, 2015].

$$\frac{\mathrm{d}}{\mathrm{dT}}\frac{\lambda_0}{\lambda} = \sum \frac{1}{\delta}\frac{\mathrm{d}\delta}{\mathrm{dT}} \tag{13}$$

$$\frac{1}{\delta}\frac{\mathrm{d}\delta}{\mathrm{dT}} = \frac{1}{\eta\, l}.\frac{\mathrm{d}\delta}{\mathrm{dT}}\,\eta\, l \tag{14}$$

Where λ_0 is a wavelength on the edge of the filter, δ is the optical thickness of the layer, η is the refractive index of the material of the layer, l is the physical thickness of the layer, and T is the temperature of the optical filter. The change in thickness of each layer constructed in the filter is summed together for the net shift in wavelength in Equation 11. Since the details of the composition of the filter and the temperature of the filter at the time of measurements is unknown, the shift in wavelength with temperature change was evaluated by observation from measurements. Lidar measurements of the backscatter signal were conducted with the filter at room temperature and with heating the filter, both on the same day. The transmittance of the edge filter across different wavelengths was compared by analysing the background signal recorded. Rotational Raman signal was not used for comparing transmittance since it depends on atmospheric conditions including local weather events and atmospheric temperature, whereas the background signal is theoretically consistent across different wavelengths, if there is no blocking of signal for any wavelengths, under similar light conditions of the atmosphere. Since the blocking filter used in our measurements limits the elastic backscatter at 355 nm and shorter wavelengths, the trend of transmittance across different wavelengths between the passbands and blocked bands, and within these bands,

should be consistent in the case of ideal filter performance which does not vary with temperature changes.

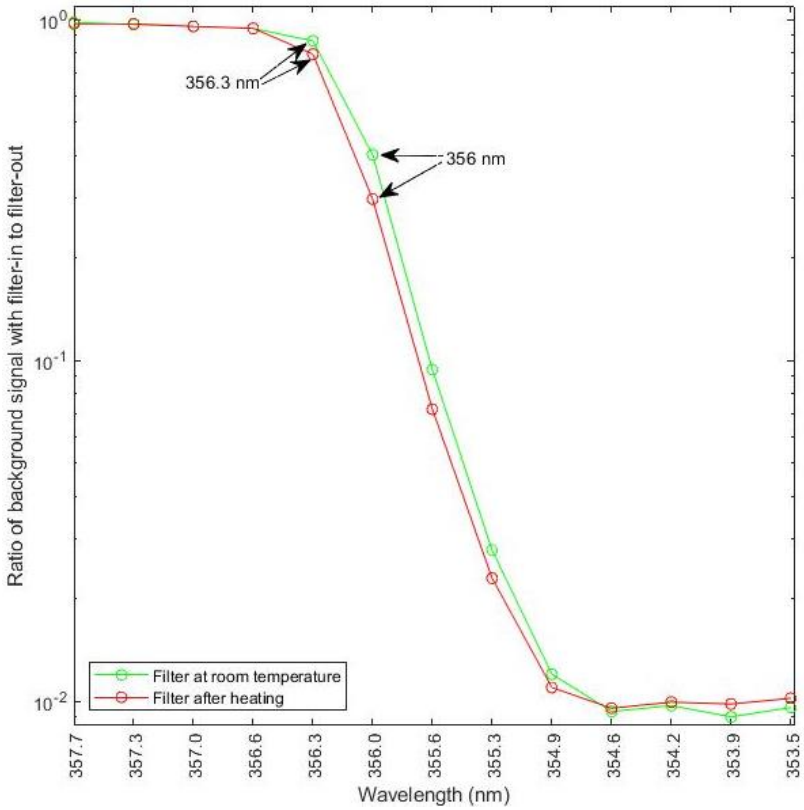

Figure 3.9. Background signal across the wavelengths on the edge of filter on June 6, 2019 under different temperature conditions of the filter- heated and without heating. The wavelengths corresponding to the blocked bands at wavelengths 355 nm or shorter. The transition slope (edge) between the pass region and blocked region lie between wavelengths 356.6 nm to 354.9 nm.

The background signal recorded by the detector decreases by 8.57% for channel 24 corresponding to the wavelength at 356.3 nm and by 25.71% for channel 25 corresponding to the wavelength at 356 nm, which reflects the decrease in transmittance across the wavelengths on the edge of filter with an increase in temperature of the filter as seen in Figure 3.10. The measurements were conducted back-to-back on the same day. Changes in the background light from the atmosphere and the weather conditions between the two measurements, if any, were accounted for by normalizing the transmittance of the passbands

for each dataset. This confirmed the temperature dependence of the transmittance of the filter across all 32 wavelengths recorded by the detector. The effect of temperature on the filter transmittance for different wavelengths was further analysed by comparing the background signal from measurements conducted on different days with varying temperature conditions in April and June in 2019. The background signal was first normalized for the passband region before comparing between the days, as shown in Figure 3.11. The measurements were all conduced in the evening after dark.

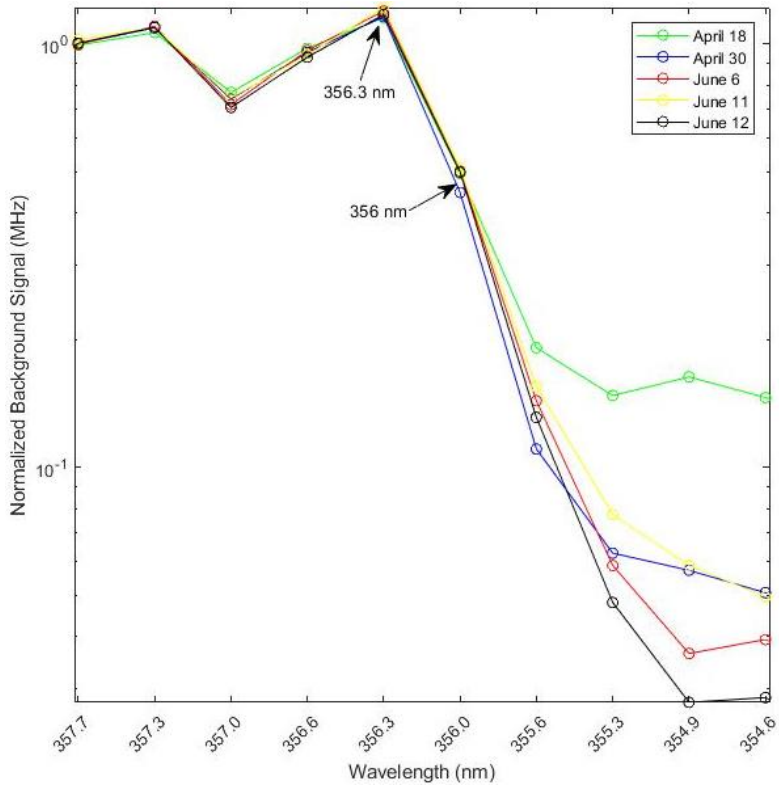

Figure 3.10. Background signal normalized for the passbands and shown for wavelengths on the edge of the filter on different days with varying outside ground temperatures in April and June in 2019.

The varying normalized background signal in Figure 3.11 confirms the transmittance dependence of the filter between measurements conducted under different temperatures of the edge filter. It was found that the filter transmittance changes substantially between the 5 days

with varying temperature conditions. The range of percentage change in recorded background signal between different days is as large as 18.4% for the signal at 356 nm at channel 25 and 8.7% for 356.3 nm at channel 24 between April 18 and June 12. The ground temperatures recorded at the time of measurements in Toronto for April 18, April 30, June 6, June 11 and June 12 in 2019 were 17º C, 8.2º C, 18.6º C, 17.2º C and 19º C, respectively. Since the ratio of rotational Raman signals is used for the derivation of atmospheric temperature, the change in transmittance as the ratio of background signal recorded in adjacent channels was evaluated and is shown in Figure 3.12.

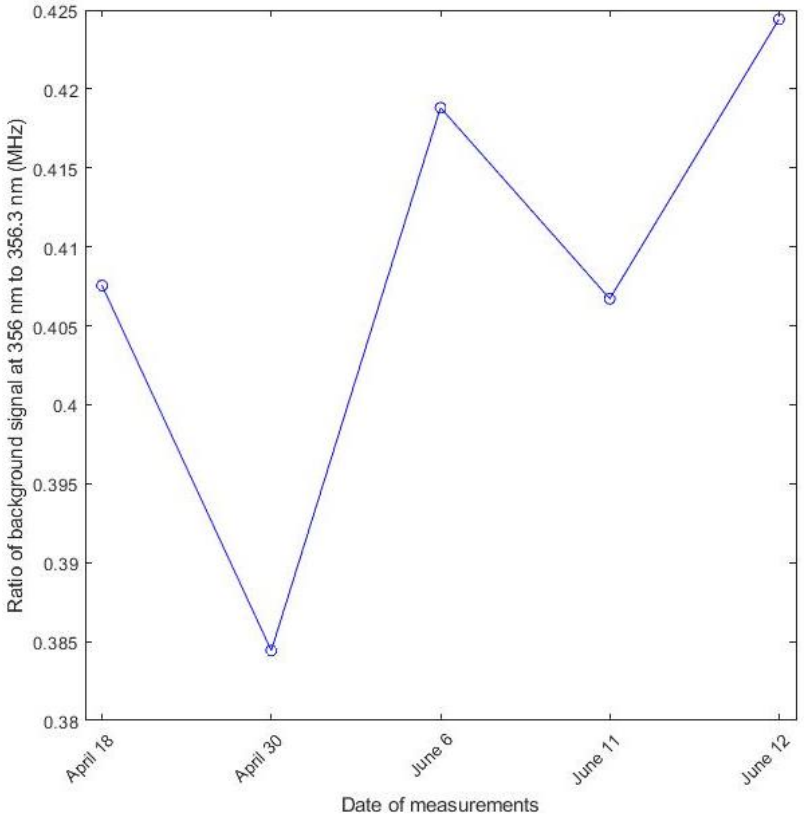

Figure 3.11. Ratio of background signal at Raman wavelengths 356 nm to 356.3 nm on different days in April and June in 2019.

The ratio of background signal at Raman wavelengths 356 nm to 356.3 nm used in the temperature derivation varies slightly between the different days of measurements, as seen in above plot. This change in signal ratio is most along the wavelengths in the blocked regions

(shorter than 355 nm) and on the edge of the filter (wavelengths longer than 355 nm, next to the elastic channel). Since the ratio of Raman signal on June 6, 2019 is used for the calibration of temperature and lidar signal to derive temperature for other days, the change in transmittance effective in the signal ratio for different days of measurements is compared and corrected against the June 6 signal ratio value. The change in transmittance for different measurements is calculated as the difference in the background signal ratio recorded at wavelengths 356 nm and 356.3 nm. This background signal ratio at Raman wavelengths was recorded as 0.418 on June 6, 2019, while the ratio decreased by 2.5% on April 18, 8.2% on April 30, and 2.7% on June 12. The background signal ratio at the two Raman wavelengths increased on June 11 by 1.3% from the June 6 ratio. The ratio of transmittance in Raman channels decreases most on April 30, which had the coldest recorded temperature in the dataset, lower than June 6 by 10º C. The ratio of transmittance increased very slightly on June 11, which was warmer than June 6 by 1º C. This reflects a decrease in transmittance at the 356 nm channel under higher temperature conditions and an increase under colder temperature conditions relative to June 6. A shift in the central wavelength of the edge filter toward longer wavelengths with increasing temperature explains the decrease in transmittance of the wavelengths, including the 356 nm channel, lying on the slope of the edge. This aligns with the theoretical expectation for the shift in wavelength with temperature change for materials with a positive temperature coefficient, as explained previously. However, the change in transmittance as effective in the signal ratio at the 356 nm and 356.3 nm is not very linear with the change in recorded outdoor temperature at the ground level. Also, the actual temperature of the filter at the time of measurements is unknown. Therefore, the correction for change in transmittance was applied using the specific percentage change for each set of measurements, instead of predicting the amount of change based on the temperature relative to June 6, 2019.

The correction for the difference in the transmittance effective in the ratio of Raman wavelengths at 356.3 nm to 356 nm was performed as below, with the normalized background signal on June 6, 2019 as the reference for correction on other days. This correction was applied to the Raman signal ratio at all height levels 'z'.

$$\text{Transmittance correction for Day X} = \frac{\text{Normalized background signal ratio on June 6}}{\text{Normalized background signal ratio on Day X}} \quad (15)$$

$$\text{Transmittance corrected signal ratio (z)} = \text{Signal ratio(z)} \times \text{Transmittance correction for Day X} \quad (14)$$

3.4.5 Overlap Region of the Lidar

In the lidar system, the received power due to atmospheric backscatter is directly related to the range-dependent receiver and transmitter overlap function, which indicates the percentage of backscatter or reflected power contained within the receiver field of view [*Ancellet et al.,* 1986]. The field of view of the telescope collecting the backscatter signal is conical which causes it to not completely overlay with the area of signal emitted by the laser below a certain minimum height above the lidar, usually the first few hundred meters from the lidar. An incomplete signal is recorded below this minimum height, which leads to lower than actual signal values near ground. The height above which there is a complete overlap between the laser and telescope field of views is called the overlap height.

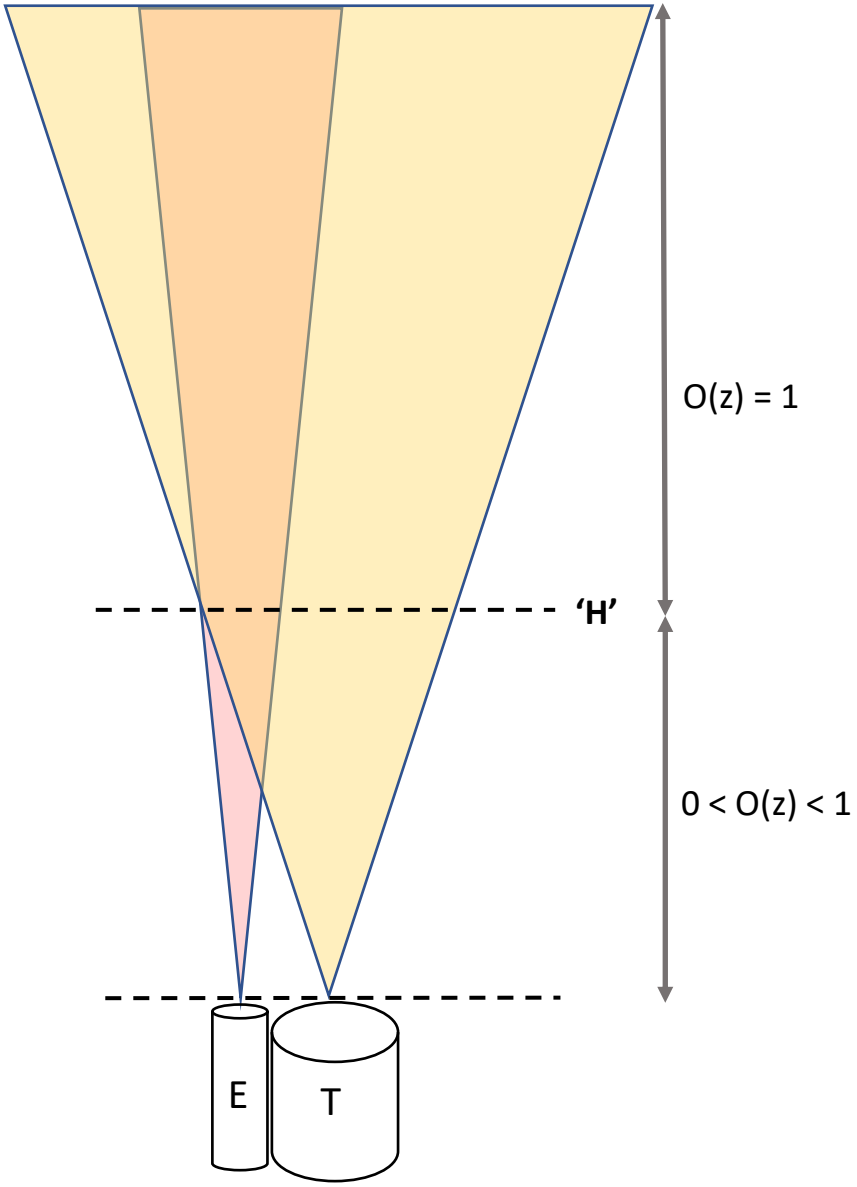

Figure 3.12. The complete overlap in field of view of laser emitter 'E' and receiver telescope 'T' occurs above a certain minimum height 'H'.

The overlap function, *O(z)*, is the fractional area of the laser beam cross-section that is inside the telescope field of view as a function of height *z* as shown in Figure 3.8. Above the overlap height, *H*, the receiver field of view and transmitted beam are completely overlapping and the signal collection efficiency is unity. Since the measurements used in this analysis are within the first 2 km from ground level, the incomplete overlap can impact the lidar signal at low altitudes and may contribute to the signal level being lower than expected. The region of

complete overlap for the lidar setup was found using the scattering ratio, derived from the theoretical molecular backscatter signal explained below.

The backscatter signal received by the lidar can be described by a mathematical equation discussed in this section. The expected signal is assumed to be the pure backscatter signal from the atmosphere. The ratio of the theoretically expected signal as a function of height and the measured lidar backscatter signal is called the scattering ratio, which is 1 in the region of complete overlap, lower than 1 in the region of incomplete overlap and greater than 1 for elastic signal when there is contribution to scattering from aerosols. The molecular lidar signal as a function of height is given by Equation 13 [*Stoyanov et al.,* 2012]. This is the 'lidar equation' and it applies to all atmospheric constituents.

$$S(z) = C\frac{A}{z^2}\,\beta_{total}\exp\left[-2\int_0^z a_{total}(z)\,dz\right] \tag{16}$$

The lidar constant *C* along with the area of the receiver *A* takes into account characteristics of the lidar setup such as the laser power, system efficiency, pulse width of the laser and the optical throughput, which are constant for all measurements performed given no system or hardware changes are made to the instrument. Optical throughput is a quantitative measurement of the amount of light passed through the system via lenses and other components within the instrument, relative to the incident light. The system efficiency is a measure of the optics and electronics in the detector, and varies between 0 to 1, where 1 corresponds to a system with no energy loss. The solid angle of the receiver aperture is A/z^2, viewed from the height of scattering, which decreases as the distance from the receiver increases. The backscatter coefficient β is the fraction of the laser pulse energy scattered back toward the receiver per unit length through the atmosphere and per unit solid angle. The extinction coefficient α is the fractional decrease in the laser pulse intensity per unit length through the atmosphere due to both scattering and absorption by particles and molecules. The

atmospheric extinction has contributions from Rayleigh and Raman scattering from molecules, scattering due to aerosols, and absorption from molecules. Specifically, the absorption effects of atmospheric gases mainly depend on their absorption intensity for the laser wavelength and total gas concentration in the atmosphere. The strongest absorption of ultraviolet light is due to molecular oxygen and ozone. While ozone is very scarce in concentration at lower heights, overall absorption is not significant by gas molecules at the 355 nm elastic wavelength. Like gas molecules, aerosols also play an important factor in the attenuation of the light through the atmosphere by absorption and scattering. While absorption by aerosols is not significant at the laser wavelengths used, given the requirement of exactly matching the energy gap for the photon to be absorbed, scattering contributions of aerosols are ignored in this analysis and only the measured elastic and Raman backscatter by molecules is used.

The backscatter coefficient and the extinction coefficient are a function of wavelength and height, however, since the wavelength of the laser pulse emitted is held constant throughout measurements, both are represented as a function of only height. The aerosol lidar ratio is the ratio of the aerosol extinction coefficient and aerosol backscatter coefficient. This combines two optical quantities that vary with height differently- aerosol constituents that vary in concentration with height and the vertically-varying relative humidity profile influences the size of aerosol particles which impacts the type and amount of scattering of photons with height [*Ackermann*, 1998]. So, the characteristic of the aerosol lidar ratio as a function of height is not constant or obvious. While scattering and absorption by both, aerosols and molecules, contribute to the extinction of light in the atmosphere, scattering is greater than absorption at the laser wavelength. The total extinction coefficient can then be calculated as $'\mathbf{a_{total}}(\mathbf{z}) = \mathbf{a_{molecular,scattered}}(\mathbf{z})'$. The ratio of the molecular extinction coefficient to the molecular backscatter coefficient is constant for a given wavelength over a

wide range of altitude, assuming contribution from scattering only. This is true for near-ground levels used in this analysis where the atmospheric absorption of light is negligible relative to the scattering. This ratio is called the molecular lidar ratio and is calculated as shown in Equation 14 [*Liou*, 2002].

$$\text{Molecular Lidar Ratio (z)} = \frac{a_{molecular}(z)}{\beta_{molecular}(z)} = \frac{8\pi}{3} \tag{17}$$

The total molecular extinction coefficient depends on the vertically resolved values of molecular number density, temperature and pressure. The extinction coefficient is given by below equation [*Liou*, 2002].

$$\mathbf{a_{total}(z) = \sigma_s \,.\, N(z)} \tag{18}$$

where σ_s is the scattering cross-section area which represents the amount of energy incident on a molecule that is scattered away from the original direction because of a scattering event that redistributes the energy isotopically over the area of the molecule [*Liou*, 2002]. The atmospheric molecular number density as a function of height, represented as *N (z)*, is directly proportional to the amount of scattering and is expected to decrease with altitude, although not uniformly through Earth's atmosphere. These can be represented as below [*Liou*, 2002].

$$\sigma_s = \frac{8\pi^3}{3} \cdot \frac{(n_S{}^2-1)^2}{\lambda^4 N^2{}_{SO}} \cdot \frac{6+3\gamma}{6-7\gamma} \tag{19}$$

$$N(z) = \frac{N_a}{R} . \frac{P(z)}{T(z)} \tag{20}$$

A correction factor γ is incorporated in Equation 16 to account for the anisotropic property of molecules because of which the refractive index of molecules varies along the x, y and z directions with an anisotropic factor of γ = 0.035. N_{so} is the volume number density of

molecules at standard atmospheric temperature and pressure conditions and is calculated to be 2.55 x 10^6 per m^3. The wavelength λ is that for which the extinction coefficient is being calculated, which is 355 nm for elastic scattering, and 356.3 nm and 356 nm respectively for the two Raman scattering cases. The atmospheric refractive index n_s is a function of air pressure, absolute temperature, and humidity, and is very close to 1. The value is around 1.00035 near the Earth's surface and decreases with height since it is inversely proportional to temperature and directly proportional to pressure and humidity. However, the change in the refractive index is very small to influence the net value in Equation 15 and remains mostly constant throughout large vertical ranges. A finer evaluation in the change in n_s can be done by measuring refractivity. The molecular number density *N(z)* at each height is a function of the pressure and temperature values at that level, and is calculated using the ideal gas relationship and the interpolated parameter data values from radiosonde measurements conducted in Buffalo. The vertical density profile is calculated in incremental values starting at the molecular number density at ground, calculated using temperature and pressure values at ground, T_0 and P_o, respectively. *R* is the universal gas constant and N_a is Avogadro's number. Optical depth is a measure of scattering of radiation by an optically active medium, in this case the atmosphere, as a function of height and is calculated as the integral of the extinction coefficient. The extinction term, $a_{total}(z)$, backscatter coefficient $\beta_{total}(z)$ and optical density as a function of height, *OD (z)* are calculated using below equations [*Liou,* 2002]..

$$\mathrm{a_{total}(z)} = \frac{8\pi^3}{3} \cdot \frac{({n_S}^2-1)^2}{\lambda^4 {N^2}_{SO}} \cdot \frac{6+3\gamma}{6-7\gamma} \cdot \frac{N_a}{R} \cdot \frac{P(z)}{T(z)} \tag{21}$$

$$\mathrm{\beta_{total}(z)} = \frac{\pi^2}{\lambda^4} \cdot \frac{({n_S}^2-1)^2}{{N^2}_{SO}} \cdot \frac{6+3\gamma}{6-7\gamma} \cdot \frac{N_a}{R} \cdot \frac{P(z)}{T(z)} \tag{22}$$

$$\mathrm{OD(z)} = \frac{8\pi^3}{3} \cdot \frac{({n_S}^2-1)^2}{\lambda^4 {N^2}_{SO}} \cdot \frac{6+3\gamma}{6-7\gamma} \cdot \frac{N_a}{R} \cdot \int_0^z \frac{P(z)}{T(z)}\, dz \tag{23}$$

The ability of the atmosphere to allow electromagnetic radiation to pass through it is called transmittivity, which is measured by the spectral transmittance for a particular wavelength. In a homogenous environment, spectral transmittance is independent of the minor layering inconsistencies in the atmospheric levels and is calculated as the exponent of the optical density (OD), given by Equation 24. Both, the extinction coefficient and transmittance are expected to decrease with altitude, with the latter being close to 1 at ground, as seen in Figure 3.13 and 3.14. The exponential term in the lidar equation is the round-trip transmittance of the atmosphere, which is the square of the transmittance, shown in Equation 25.

$$\mathrm{T}(z) = e^{-OD} \tag{24}$$

$$\mathrm{T}^2(z) = \exp\left[-2\int_0^z a_{total}(z)\right] \tag{25}$$

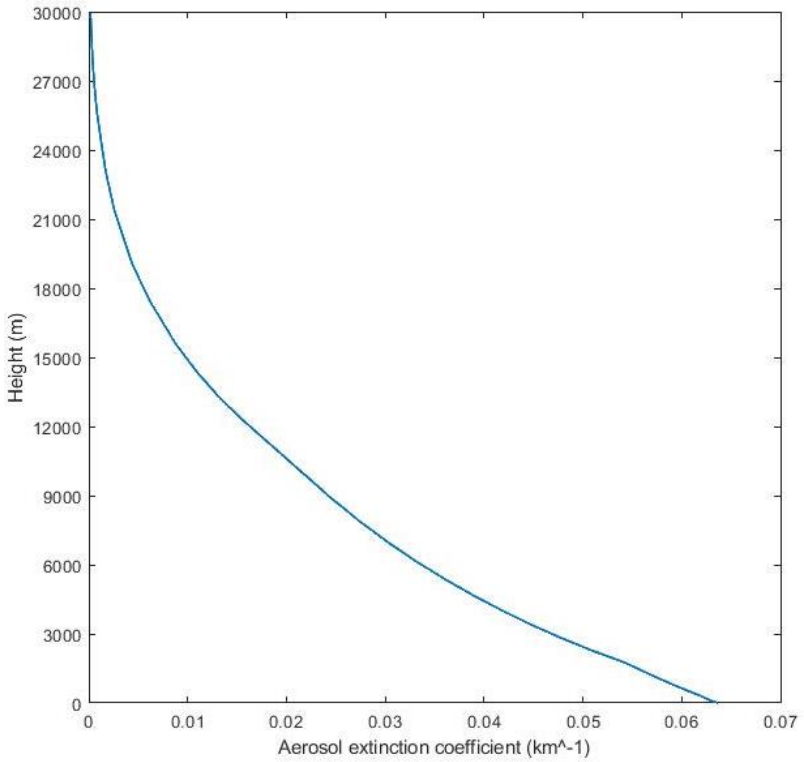

Figure 3.13. Total extinction coefficient of the atmosphere at 355 nm on June 6, 2019 at York University, calculated using temperature and pressure values from radiosonde measurements.

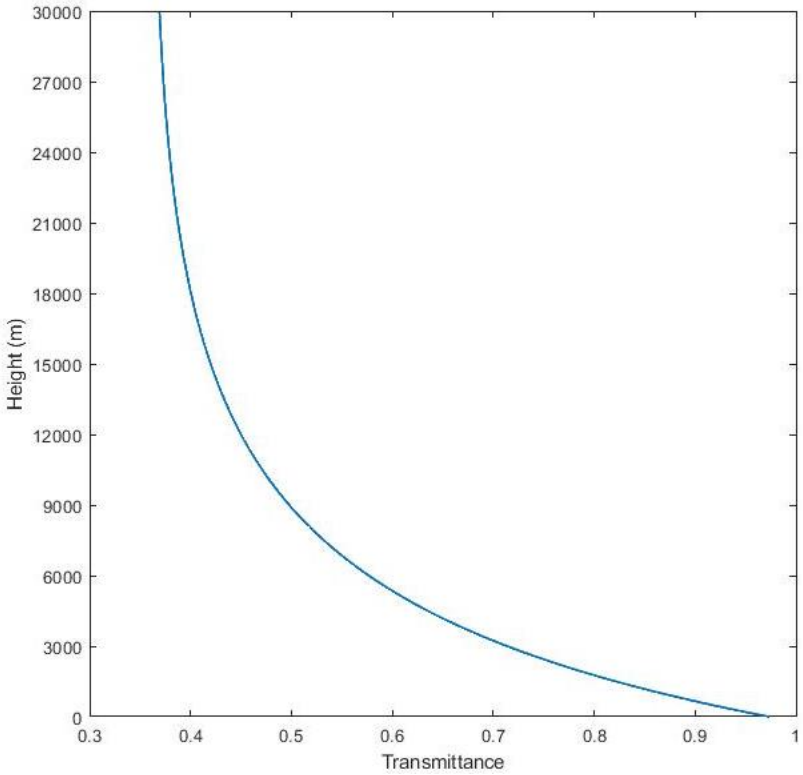

Figure 3.14. The transmittance of the molecular atmosphere from the ground toi the indicated height derived from the vertical integral of the extinction function.

Inputting the round-trip transmittance and the backscatter-extinction coefficient term in the lidar equation gives the expected backscatter signal represented in Equation 26.

$$S(z) = C\frac{A}{z^2}\,\pi^2.\frac{(n_S{}^2-1)^2}{\lambda^4\,N^2{}_{SO}}.\frac{6+3\gamma}{6-7\gamma}.\frac{N_a}{R}.\frac{P(z)}{T(z)}.\mathrm{T}^2(z) \qquad (26)$$

The recorded backscatter signal from lidar measurements divided by the theoretical, pure molecular backscatter signal *S(z)* defines the scattering ratio of measured lidar signals at different altitudes. The pure molecular signal is normalized to the measured Raman signal at higher altitudes where the overlap is complete. The profile for the measured backscatter signal and theoretical molecular signal at 356.3 nm is plotted in Figure 3.15, and the scattering ratio for the same is plotted in Figure 3.16. It is observed that the scattering ratio is less than unity from ground up to 280 m. In this range, the recorded lidar signal is lower than expected due to the incomplete overlapping of the emitted light beam and detected light beam

because of the instrument geometry. As the overlap between these two areas increases with altitude, the ratio also increases and is unity beyond the overlap height. For elastic signal at 355 nm, due to the higher aerosol concentration near ground that contributes to increased scattering of the laser light, the ratio of the measured to molecular signal is greater than 1 even below the minimum height of complete overlap. As the aerosol concentration decreases with increasing altitude, the ratio decreases beyond this point before merging to unity in the region of mostly molecular atmosphere and complete overlap, as seen in Figure 3.17.

Therefore, the minimum height above which the overlap for the lidar Raman signals is complete is detected at 280 m. The analysis for temperature derivation using Raman backscatter signal could include deviations below 280 m due to the incomplete overlap of the emitter and detector.

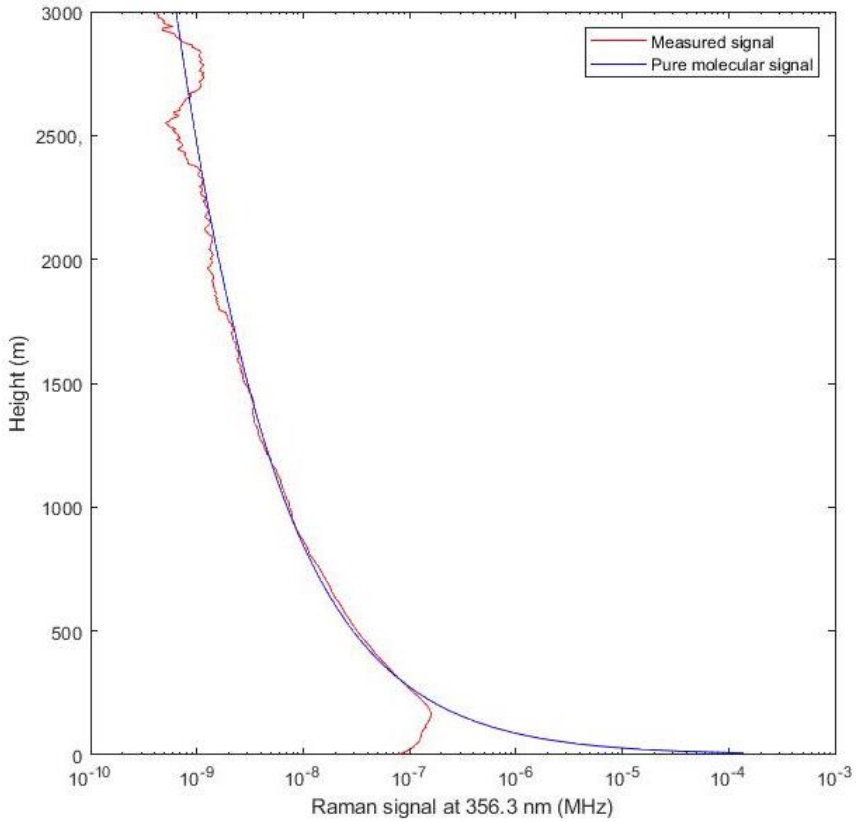

Figure 3.15. Lidar measured backscatter signal and normalized pure molecular signal for Raman wavelength at 356.3 nm on June 6, 2019.

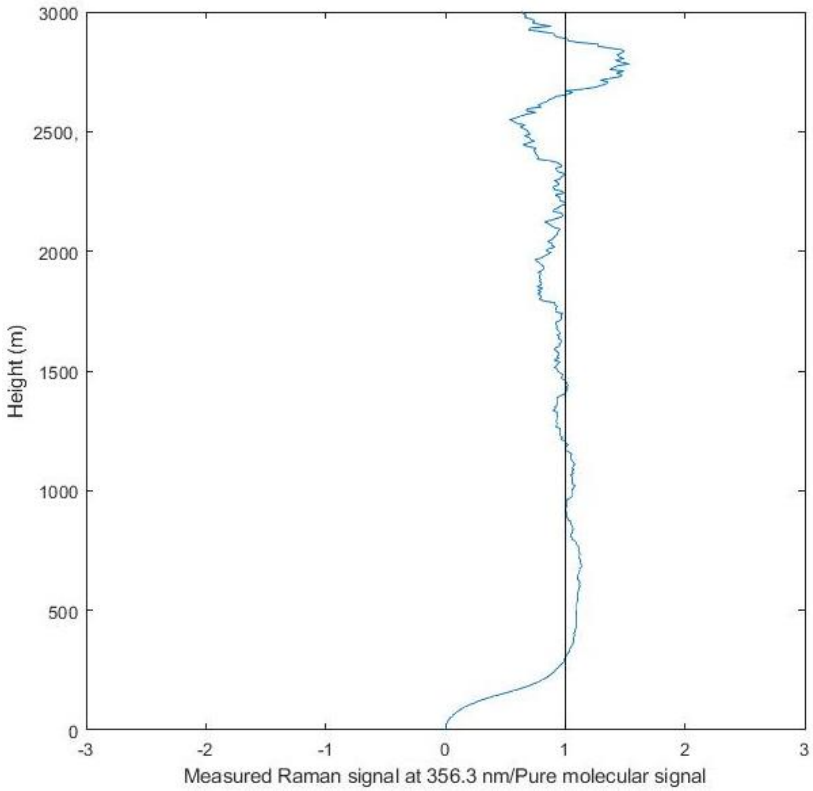

Figure 3.16. Scattering ratio for Raman wavelength at 356.3 nm on June 6, 2019. The minimum height for complete overlap is detected at 280 m.

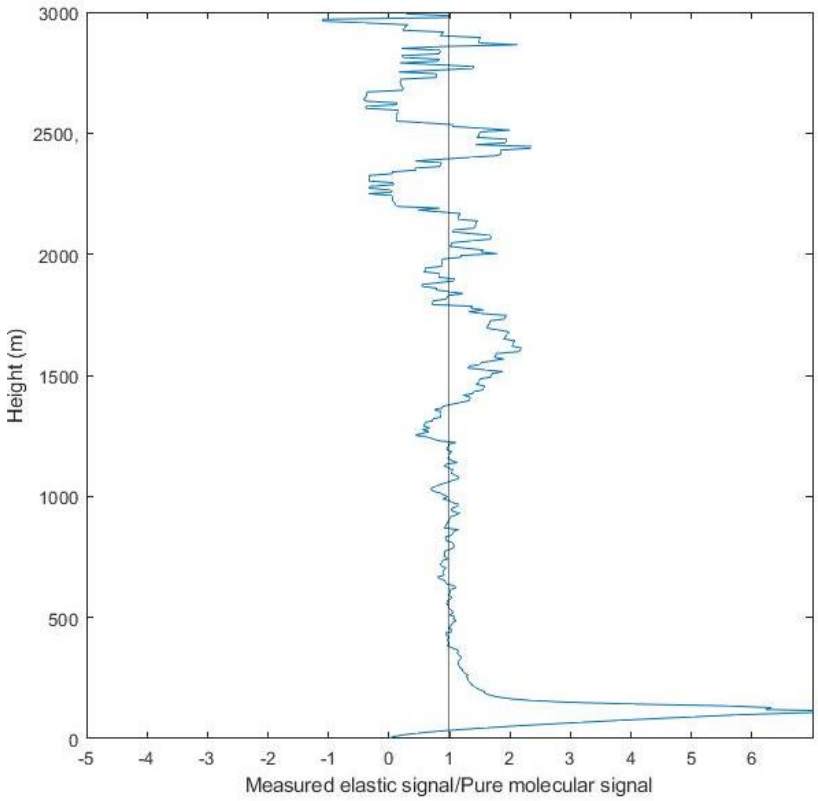

Figure 3.17. Scattering ratio for elastic wavelength at 355 nm on June 6, 2019 reflects larger scattering near ground due to higher aerosol concentration.

3.5. Radiosonde Data for Calibration

The calibration of temperature and rotational Raman backscatter signal ratio for measurements on one day to determine the temperature profile for another day is performed by using local atmospheric temperature data from the nearest possible accurate source. The nearest available source of vertical temperature data for the lab at York University in Toronto are the sounding measurements conducted in Buffalo, Unites States. The radiosonde data was obtained from the University of Wyoming, Department of Atmospheric Sciences website (http://weather.uwyo.edu/upperair/sounding.html). The first radiosonde measurement is recorded at around 215 m above ground and goes up to 33 km above ground, with varying vertical step-size between consecutive data points ranging from around 26 m near ground to 194 m at higher heights. The radiosonde data vertical resolution is much lower than the vertical step-size of the lidar data, so the radiosonde measurement data was linearly interpolated to the height levels of the lidar data to generate the same vertical resolution of 7.5 m. The local weather conditions between Buffalo and Toronto vary slightly as expected since the two laboratories are 75 km apart. The radiosonde observation site located at 42.93º N, while the York University laboratory is located at 43.46º N. The expected average temperature difference between the two locations is around 0.473º C from theoretical latitudinal temperature change calculation [*La Sorte et al.,* 2014]. The difference in the recorded ground temperature between the two locations in the duration of measurements is 6.6 K on April 18, 2.2 K on April 30, 4.8 K on June 6, 0.4 K on June 11, and 7.1 K on June 12, with Buffalo being slightly warmer than Toronto except on June 11. The difference in ground temperature between Buffalo and Toronto is accounted for by subtracting the difference from the radiosonde temperature values at all heights before interpolation. This provides a linear correction which should be accurate since the temperature gradient is approximately constant within the boundary layer.

The starting height level for the radiosonde measurements in Buffalo is 215 m above sea level, which corresponds to 15 m above ground at York University due to the altitude offset at both locations. This height offset was accounted for before interpolation of data so that the vertical levels in the two datasets match. The radiosonde data was extrapolated to correspond to a start-level at ground from the lidar.

Chapter 4.

Temperature Derivation

4.1. Lidar Ratio- Radiosonde Temperature Function Fit

Radiosonde temperature data from the sounding location in Buffalo (station number 72528) was downloaded from the University of Wyoming, Department of Atmospheric Science website. To check for the accuracy of the use of Buffalo temperature data for the calibration function of temperature in Toronto, ERA reanalysis model data for Toronto from ECMWF was compared to the radiosonde temperature data. The ERA datasets are climate reanalysis products, a process that gives a numerical description of the recent climate by combining models with observations. The reanalysis uses data assimilation, a process by which observations of a system are incorporated into the model state. A numerical model, based on past trends and including coupling effects between the state variables determines how the model parameters change with time. A new product, ERA 5 was used for comparison with radiosonde data because it has an increased resolution of 31 km worldwide, hourly availability of parameter data values and is the first reanalysis model to include an uncertainty estimate from a 10-member ensemble of data assimilations. The dataset for ERA5 was downloaded for 43.75º N and 79.5º W, the closest available coordinates to York University. The temperature in the radiosonde dataset starts at 292.22 K at ground, whereas the ERA5 dataset starts at 293.92 K at ground. The deviation in temperature in both datasets decreases with height and the trend of temperature change with height is congruent, as observed in Figure 4.1. The average temperature recorded at Pearson airport in Toronto on

June 6, 2019 is 292.67 K between 8 pm to 10 pm, which is closer to the temperature recorded in the radiosonde data and not ERA5. The average vertical resolution of the ERA5 dataset is 226.90 m in the height range of interest, whereas the average resolution for the radiosonde dataset is 141.92 m. The radiosonde measurements remain within the 1.0345 K standard deviation between the two datasets. Since the radiosonde temperature is checked for accuracy, possesses finer vertical resolution, and the temperature recorded at ground is closer to the temperature recorded in Toronto during the time of the measurement, the radiosonde data is used for temperature derivation.

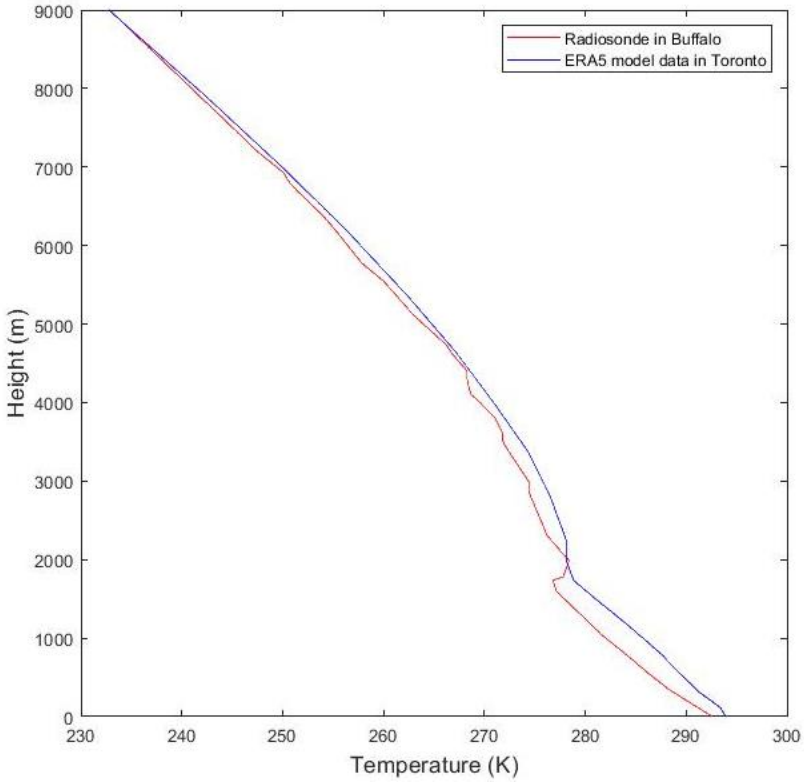

Figure 4.1. Buffalo radiosonde data and Toronto ERA5 reanalysis model data for temperature profile in Toronto on June 6, 2019.

Plotting the radiosonde temperature against the ratio of rotational Raman backscatter signal at 356 nm and 356.3 nm wavelengths is shown in Figure. 4.2. The decrease in the signal ratio with decrease in temperature is exponential at higher temperature values from

290 K to 282 K, corresponding to an altitude level of ground to up to 1200 m. The dependency of the signal ratio on temperature is noisier for values lower than 280 K, with very small change in signal ratio per degree Kelvin change in temperature along with larger variance. Therefore, for a certain range of the data, there is temperature dependence of the rotational Raman channel signal ratio that can be represented by a quadratic equation and this relationship should hold true for the signal ratio of the same two wavelengths for other days of Raman measurements. The signal ratio and temperature dataset is used to derive the function describing the temperature dependency of the rotational Raman backscatter signal ratio. Starting from Equation 9 in Section 2.2, different quadratic and cubic curve-function fits were performed using non-linear regression modelling and were analysed for best fit by comparing the respective standard deviations from the temperature-signal ratio dataset. The function with the least amount of standard deviation from radiosonde temperature data was identified as Equation 27.

$$R = ae^{b(T+d)^2} + c \tag{27}$$

In Equation 27, *T* is the temperature value from the radiosonde data, *R* is the ratio of the signal at 356 nm to the signal at 356.3 nm, and *a, b, c* and *d* are the fixed coefficients. Starting from initial estimates of the equation coefficients, the curve-fit of this function was improved by fine-tuning of the coefficients using iteration of the coefficient estimates, which were evaluated by comparison of resulting ratio function with the measured ratio values. The coefficient values for the best-fit equation found using June 6 data are 5.837×10^{-32}, 8.464×10^{-4}, 0.487, and 2.6 for *a, b, c* and *d* respectively. The output of the function fit was tested for accuracy for the same measurements using the calculated coefficient values and comparing the derived temperature profile against the radiosonde temperature data. The temperature values were found by rearranging Equation 27 to calculate a unique temperature value for

each signal ratio data value, given by Equation 28. The temperature-signal ratio data and corresponding best-fit function is shown in Figure 4.2.

$$\text{Temperature} = \sqrt{\frac{\log(\text{raman channel ratio} - \text{c}) - \log(\text{a})}{b}} - \text{d} \qquad (28)$$

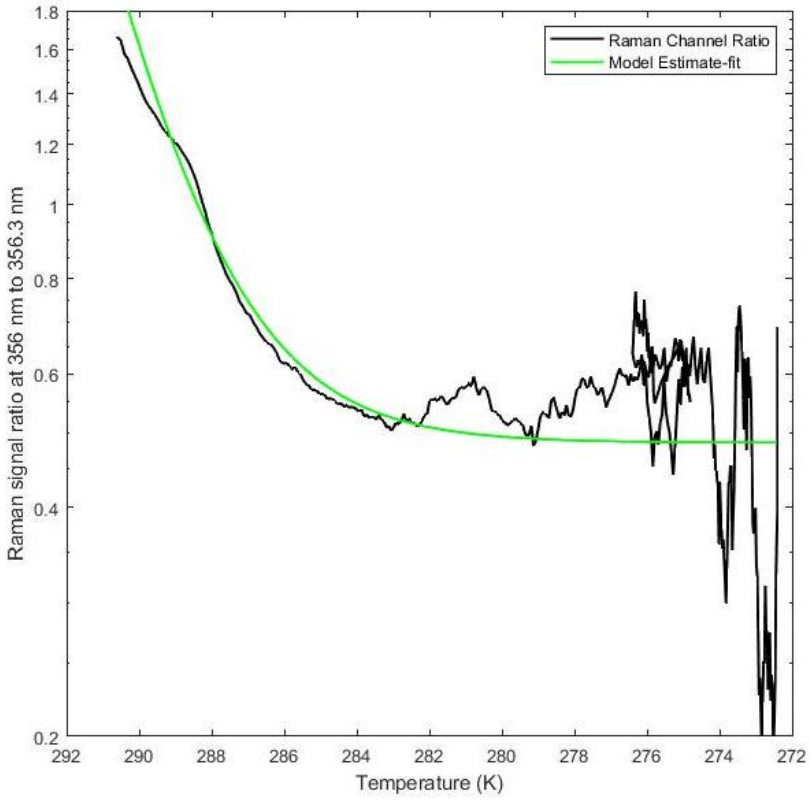

Figure 4.2. Nonlinear regression model fit to Raman channel ratio and temperature on June 6, 2019 to get the best-fit coefficients of the curve function.

The next step was to apply this calibration function to derive the temperature profile for another day using only the lidar signal ratio data from measurements performed on that day. Rotational Raman backscatter signal from lidar measurements conducted after dark on April 18, April 30, June 11 and June 12 in 2019 were used for this. The channels corresponding to the rotational Raman wavelengths at 356.3 nm and 356 nm, that were used in the calibration function for June 6, 2019, were used for the application of the function to other days. Since no changes were made to the spectral grating setting of the detector, the channels

corresponding to the wavelengths remained the same at number 24 and 25. The calibration function is applicable to temperature ranging between 282 K to 292 K. Below 282 K, the calibration function is not sensitive to temperature and is rather constant with change in temperature, as seen in Figure 4.2. This is because the signal detected above 1200 m above ground has large relative uncertainty such that the ratio is not sensitive to the small changes in temperature. The background-subtracted backscatter signal at the two Raman wavelengths after non-linearity and cross-talk correction, and correction for change in transmittance of the optical filter is plotted in Figure 4.3. The trend of decrease in Raman signal strength with altitude is consistent amongst all days, and the Raman signal at 356.3 nm has higher recorded strength relative to the signal at 356 nm. This is expected since the 356.3 nm signal is nearer to the passed band region of the optical filter relative to the 356 nm signal.

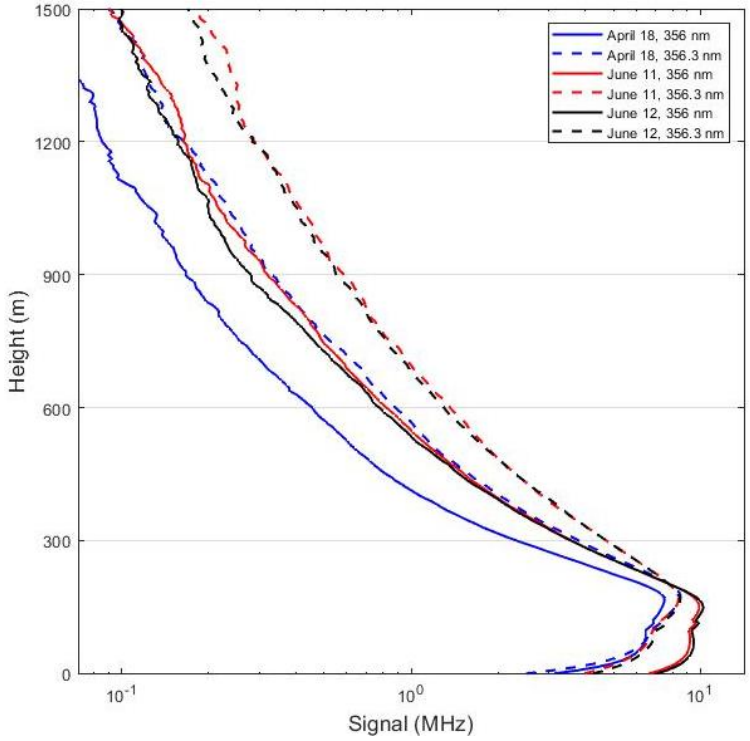

Figure 4.3. Background subtracted rotational Raman signals from lidar measurements on April 18, June 11 and June 12 in 2019 at York University.

The difference in strength of the two wavelength signals varies between days because the transmittance of the filter at 356 nm was observed to decrease more than at 356.3 nm with the

shift in wavelengths on the edge of the filter between different days of measurements. The ratio of the signal at 356 nm to 356.3 nm for different measurement days is plotted in Figure 4.4.

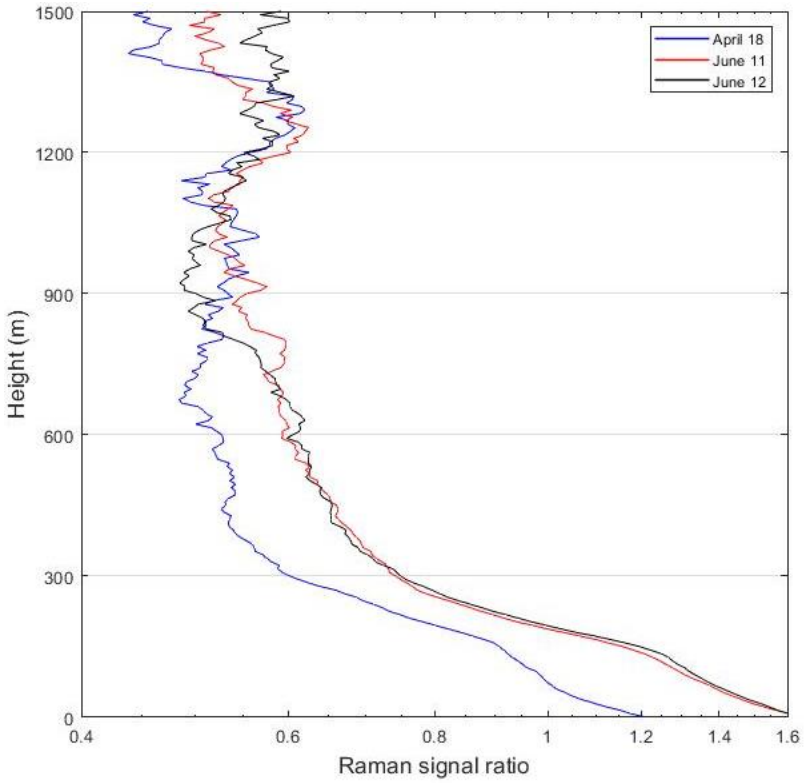

Figure 4.4. Rotational Raman backscatter signal ratio at 356 nm and 356.3 nm from lidar measurements on April 18, June 11 and June 12 in 2019.

4.2. Temperature Profile Derivation

Atmospheric temperature values were calculated using Equation 28 derived from the calibration of radiosonde data and lidar signal measurements on June 6, 2019. Applying the calibration function for other days of measurements, each input Raman signal ratio value produced a unique corresponding temperature value. The lidar signal derived temperature values were compared against the radiosonde temperature values in Buffalo, plotted below in Figure 4.5. The temperature recorded on April 30, 2019 ranges from 281 K at ground to 273 K at 1000 m above ground. The signal ratio in the calibration function is not sensitive to this

temperature range, as seen in Figure 4.2. Therefore, the derived calibration is not applicable to calculate temperature on April 30, 2019.

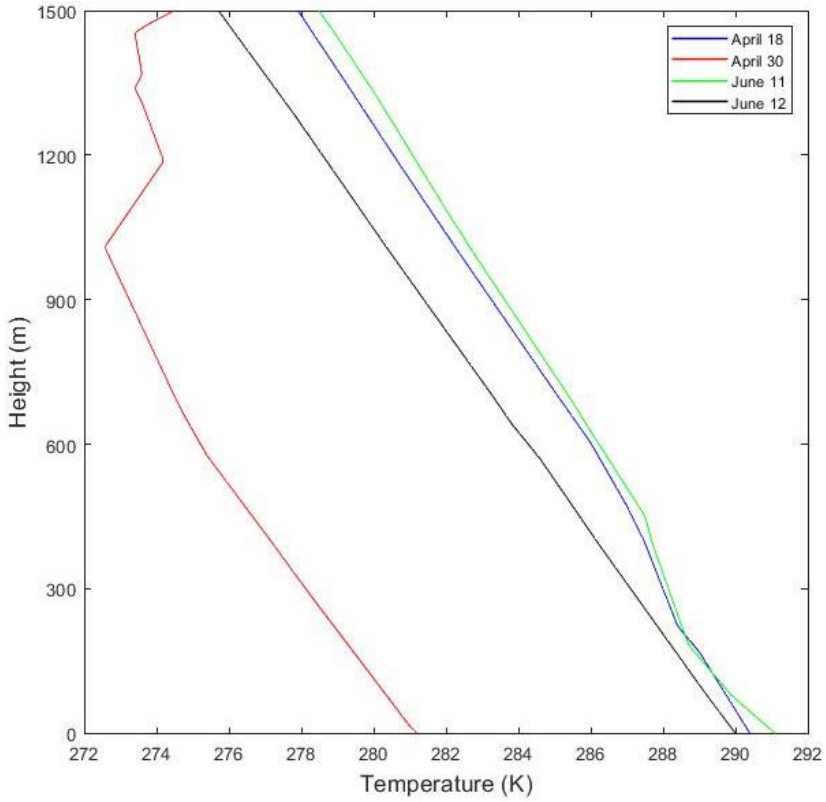

Figure 4.5. Vertical atmospheric temperature data from radiosonde measurements in Buffalo on April 18, April 30, June 11 and June 12 in 2019.

4.3. Propagation of Signal Uncertainty in Temperature Calculation

The calculation of uncertainty in the backscatter photon-counting signal is explained in Section 3.3. Starting with Equation 10 to evaluate the uncertainty in measured signal as the square root of the mean number of detected photons, the uncertainty in signal at each altitude for the Raman wavelengths at 356 nm and 356.3 nm was propagated in the calculation for lidar signal-derived temperature values given by Equation 28 using the steps below.

$$\text{error}_{\text{ratio}} = \frac{\text{Signal at 356 nm}}{\text{Signal at 356.3 nm}} \times \sqrt{\left(\frac{\text{Signal uncertainty}_{356\text{ nm}}}{\text{Signal at 356 nm}}\right)^2 + \left(\frac{\text{Signal uncertainty}_{356.3\text{ nm}}}{\text{Signal at 356.3 nm}}\right)^2} \qquad (29)$$

$$\text{Error in } `\frac{\text{signal ratio} - c}{a}' = \frac{\text{error}_{\text{ratio}}}{a} \tag{30}$$

$$\text{Error in } `\log\left(\frac{\text{signal ratio} - c}{a}\right)' = 0.434 \times \frac{\frac{\text{error}_{\text{ratio}}}{a}}{\frac{\text{signal ratio} - c}{a}} \tag{31}$$

$$\text{Error in } `\frac{\log[\text{signal ratio} - c/a]}{b}' = 0.434 \times \frac{\text{error}_{\text{ratio}}}{(\text{signal ratio} - c) \times b} \tag{32}$$

$$\text{Error}_{\text{temperature}} \text{ in } `\sqrt{\frac{\log[\text{signal ratio} - c/a]}{b}}' = \frac{0.434 \times \text{error}_{\text{ratio}}}{2 \times T \times (\text{signal ratio} - c) \times b} \tag{33}$$

An approximation for error in logarithmic values was used in Equation 32.

4.4. Results

The lidar signal-derived vertical temperature profile of the atmosphere for April 18, June 11 and June 12 in 2019 is plotted up to a height of 1200 m in Figures 4.6, 4.8 and 4.10. Beyond 1200 m above ground, the rotational Raman signal ratio at 356 nm to 356.3 nm is low and in the range of the calibration function where there is no sensitivity to temperature. The relative uncertainty in the calculated temperature values is shown using error bars in the plots. This is the uncertainty propagated in the calculated temperature values due to the uncertainty in photon-counting detection that increases with altitude on all days since the number of detected photons decreases with height, which increases the total propagated error given by Equation 33. The calculated temperature values from the equation fit for April 18, 2019 ranges from 289.13 K at ground to 284.12 K at 1200 m above ground, compared to 289.4 K and 280 K recorded by the radiosonde at those respective levels. The derived temperature in this height range decreased by a maximum of 8.32 K from ground level at 690

m altitude. The absolute error in the temperature profile, which is the difference between the radiosonde and lidar-derived temperature values, is plotted in Figure 4.7. The mean divergence of the lidar calculated temperature from the radiosonde measured values from ground to up to 1200 m is 2.34 K.

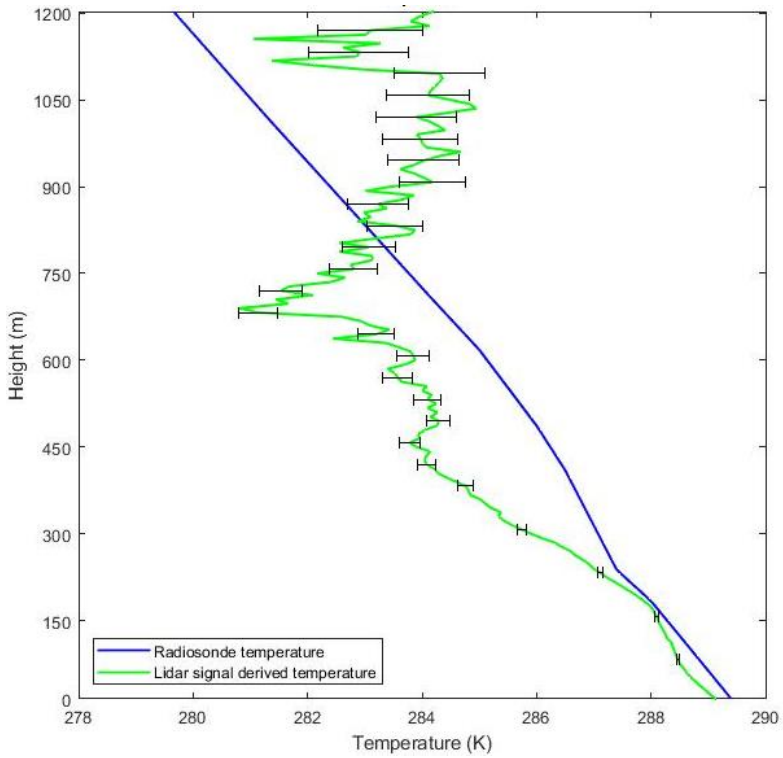

Figure 4.6. Comparison of Raman signal derived vertical temperature profile using lidar measurements in Toronto and the radiosonde temperature profile measured in Buffalo on April 18, 2019. The uncertainty in the calculated temperature is shown with error bars.

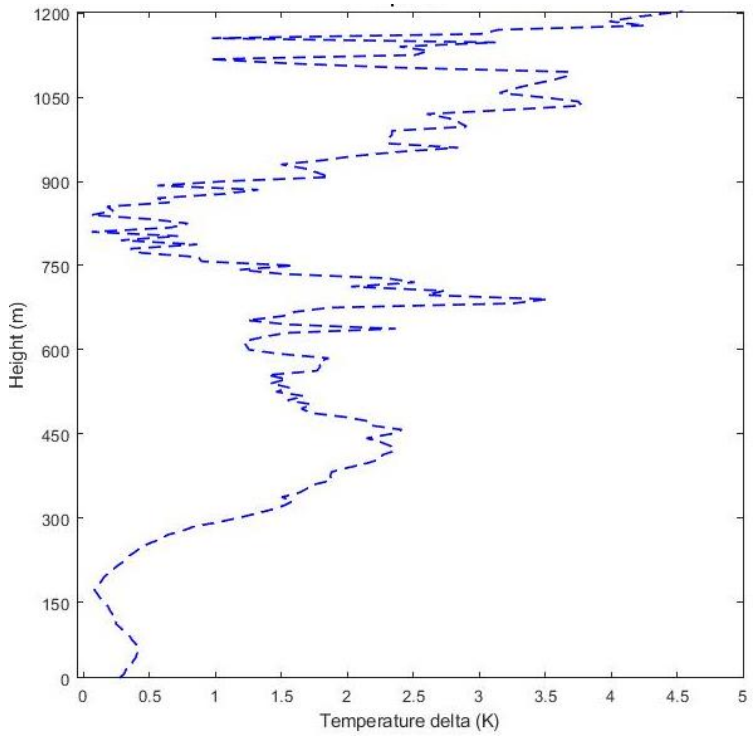

Figure 4.7. Absolute difference between the radiosonde temperature and lidar temperature values on April 18, 2019.

The lidar signal derived temperature values from the equation fit for June 11, 2019 ranges from 290 K at ground to 284.6 K at 1200 m above ground, compared to 290.6 K and 280.6 K recorded by the radiosonde at those respective levels. The derived temperature in this height range decreased by a maximum of 7.62 K from ground level at 1013 m altitude, as seen in Figure 4.8. The absolute difference between the radiosonde and lidar-derived temperature values is plotted in Figure 4.9. The mean divergence of the lidar calculated temperature from the radiosonde measured values from ground to up to 1200 m is 1.61 K.

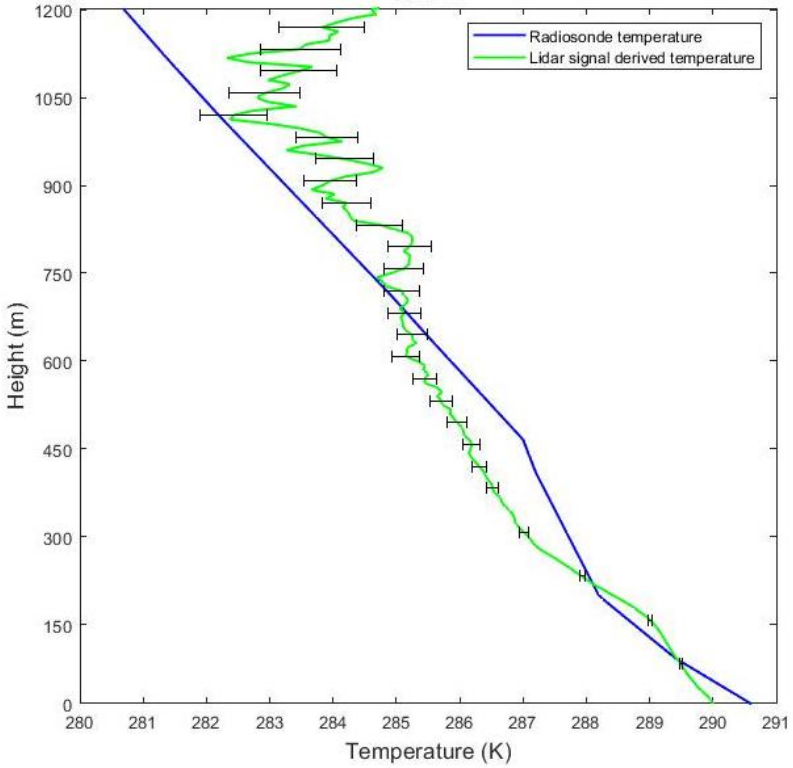

Figure 4.8. Raman signal-derived vertical temperature profile using lidar measurements in Toronto and radiosonde temperature profile measured in Buffalo on June 11, 2019.

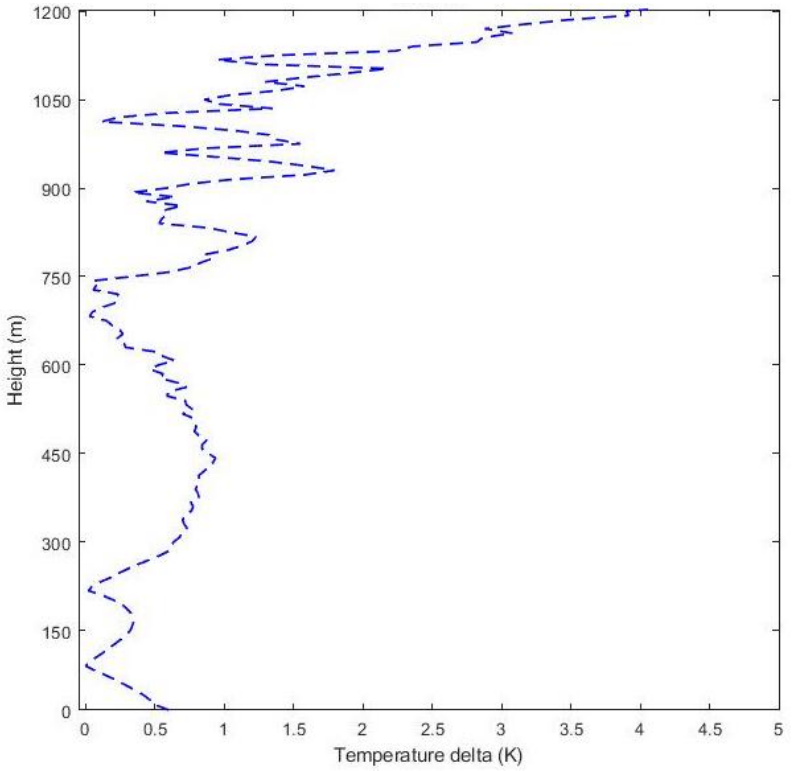

Figure 4.9. Absolute difference between the radiosonde temperature and lidar temperature values on June 11, 2019.

The lidar signal derived temperature values from the equation fit for June 12, 2019 ranges from 290.31 K at ground to 284.78 K at 1200 m above ground, compared to 290.4 K and 279.13 K recorded by the radiosonde at those respective levels. The derived temperature in this height range decreased by a maximum of 11.12 K from ground level at 938 m altitude, as seen in Figure 4.10. The absolute difference between the radiosonde and lidar-derived temperature values is plotted in Figure 4.11. The mean divergence of the lidar calculated temperature from the radiosonde measured values from ground to up to 1200 m is 2.48 K.

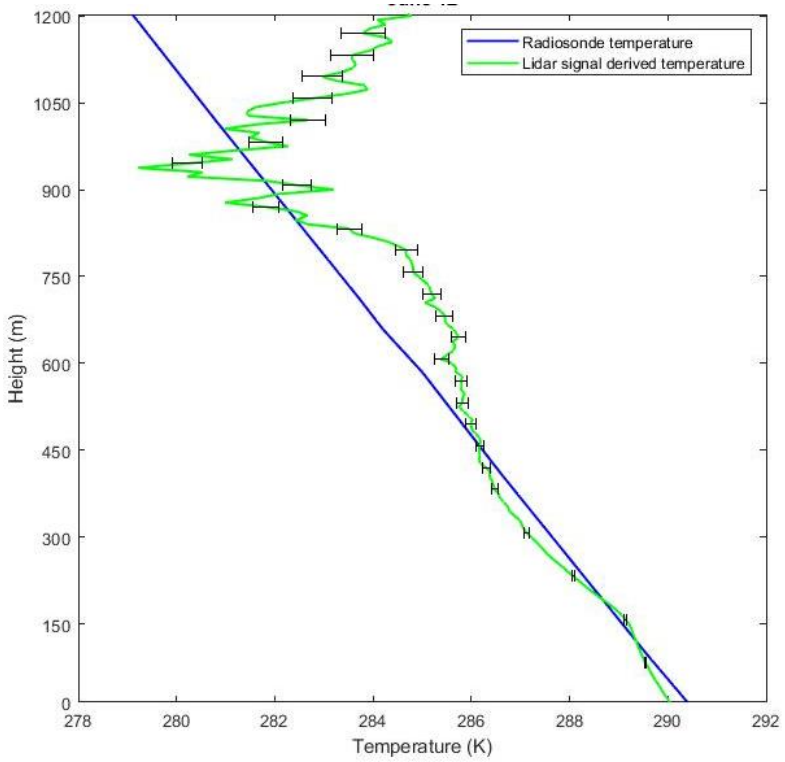

Figure 4.10. Raman signal-derived vertical temperature profile using lidar measurements in Toronto and radiosonde temperature profile measured in Buffalo on June 12, 2019.

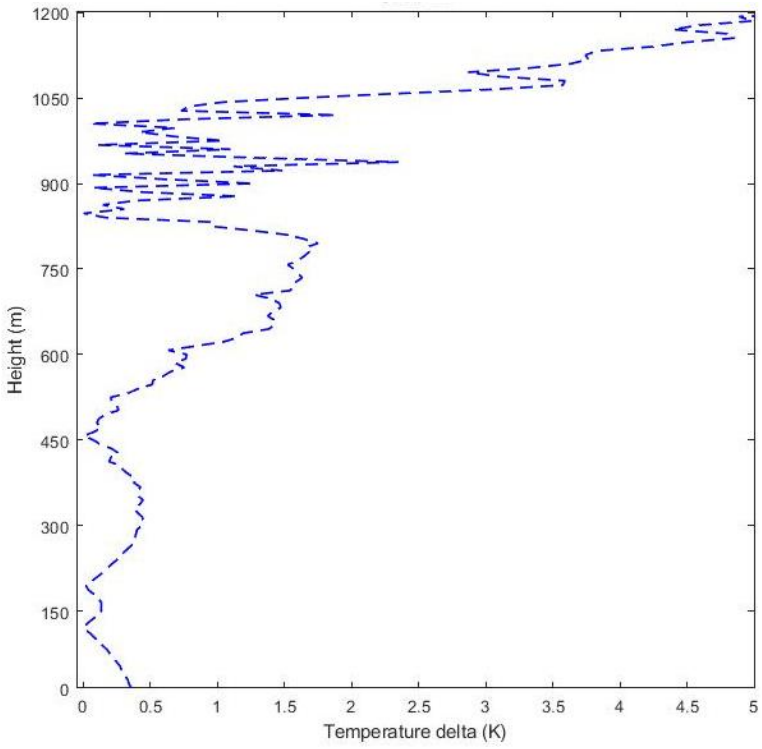

Figure 4.11. Absolute difference between the radiosonde temperature and lidar temperature values on June 12, 2019.

The derived temperature values are within ± 3 K of the radiosonde temperature values up to a height of 1000 m for all three days, except for briefly around 680 m on April 18. The relative uncertainty in the calculated temperature values is within ± 1 K margin for all three days up to a height of 1000 m. The atmospheric temperature gradient was the highest on June 12 and least on April 18 for both, the lidar-derived values and radiosonde values, compared to all the measurement days included in the analysis. Overall, the rotational Raman derived temperature profile for Toronto reflects the same trend in temperature decrease with altitude as the sounding measurement data in Buffalo on April 18, June 11 and June 12 in 2019, with a mean error margin of 2.14 K up to 1200 m above ground.

Chapter 5.

Conclusion

The purpose of this analysis was to test the novel combined used of a ground-based lidar system with the Licel 32-channel multispectral detector to derive vertical atmospheric temperature profile from rotational Raman backscatter signal measurements, which was accomplished. The objective of the deriving vertical temperature values within ± 1 K relative uncertainty margin was achieved for up to 1000 m above ground. The absolute uncertainty or the difference between the lidar-derived temperature values and radiosonde temperature values for April 18, June 11 and June 12 in 2019 was within ± 3 K up to a height of 1000 m. The analysis was successful in achieving the desired relative uncertainty, but the absolute uncertainty was 2 K greater than desired. The calibration function derived from one set of local temperature measurements and the lidar rotational Raman backscatter measurements on a day were used to develop a temperature profile within a mean error margin of 2.14 K up to 1200 m above ground for other days without requiring any local weather parameter measurements. Corrections to the recorded backscatter signal including non-linearity correction of the photon-counting signal due to inherent characteristic of the photomultiplier tube, and correction for the cross-talk between channels due to leakage of signal in adjacent channels of the lidar detector were applied in this analysis.

The calibration function found using lidar signal measurements and radiosonde temperature measurements on June 6, 2019 applies to temperature in the range of 282 K to 292 K, and is not sensitive to temperature below 282 K, as discussed in the Section 4. The

main reason for this was the photon-counting signal detected at higher altitudes, corresponding to lower temperature values, had large relative uncertainty. The laser strength is the main factor limiting the signal strength at higher altitudes which directly impacts the backscatter signal ratio at the two selected Raman wavelengths in the calibration function. Using a detector system with greater laser pulse energy would allow less noisy backscatter signal measurements at greater altitudes to expand the range of measurements applicable to the calibration function to a larger range of temperature values. With the given laser strength, a more accurate calibration function can be achieved by using multiple-day measurements to establish a stronger temperature-dependency of the backscatter signal ratio of the same two Raman wavelengths and over a larger range of temperature values. Using lidar Raman signal measurements on cold, winter days in combination with the existing measurements from summer or including even warmer days will increase the temperature range of calibration function applicability. However, a decision was made to use one set of lidar measurements from a single day to test the applicability of the calibration function to derive temperature for other measurement days to provide a stronger test of the employed method. The deviation in the lidar signal-calculated temperature and local temperature values can be reduced by the locating the lidar nearer to the radiosonde launch site. In the case of measurements with our lidar system, either the instrument setup can be placed at the Buffalo sounding station or local atmospheric measurements can be conducted at York University for better coupling of the two datasets to remove the deviation caused by localised weather events and temperature differences especially at ground levels. Currently, radiosonde measurements are not conducted at or in the vicinity of the York University campus.

One of the initial problems observed during the analysis of the backscatter signal was that the measured ratios between the rotational Raman wavelengths were not consistent between different set of measurements. Looking into possible reasons for this, it was found

that this discrepancy was due to the temperature response of the edge filter. Although correction for the change in transmittance of wavelengths measured by the detector due to change in temperature of the optical filter was applied, there is still some added uncertainty. The correction was applied by simply evaluating the change in normalized background signal ratio at the two Raman wavelengths during different sets of measurements. However, the shift in the filter profile was found to still be large enough to influence the transmittance of the measured wavelengths. This correction can be enhanced by evaluating the actual numeric shift in the wavelengths on the edge of the filter with change in temperature. This would require measuring the temperature of the optical filter before collecting the lidar signal data on each day and knowing the composition of the filter components, including the thickness of the constructed layers of components and the index of refraction of the material used. This issue can be further mitigated by selecting wavelengths that do not lie on the edge of the filter, however, the selection of Raman wavelengths for strong signal strength and optimized temperature dependency may be compromised. An alternative and more concentre solution would be to prevent the temperature change of the filter by insulating it in an enclosure to hold the temperature constant.

References:

Ackermann, J. (1998). Two-Wavelength Lidar Inversion Algorithm for a Two-Components Atmosphere with Variable Extinction-to-Backscatter Ratios, *Applied Optics,* Vol. 37, Iss. 15.
doi: 10.1364/ao.37.003164

Ancellet, G., Kavaya, M. J., Menzies, R., Brothers, A. (1986). Lidar Telescope Overlap Function and Effects of Misalignment for Unstable Resonator Transmitter and Coherent Receiver, *Applied Options,* Vol. 25, Iss. 17.
doi: 10.1364/ao.25.002886

Behrendt, A. (2005). Lidar Temperature Measurements with Lidar, *Springer Series in Optical Sciences,* Vol. 102, edited by Claus Weitkamp.
doi:10.1007/0-387-25101-4_10

Behrendt, A., Nakamura, T., Tsuda, T. (2005). Combined Temperature Lidar for Measurements in the Troposphere, Stratosphere and Mesosphere. *Applied Optics,* Vol. 43, Iss. 14.
doi: 10.1364/AO.43.002930

Bevington, P.R., Robinson, D.K. (1993). *Data Reduction and Error Analysis for the Physical Sciences,* McGraw-Hill, New York.

Clemesha, B. R., Kent, G.S., Wright, R.W.H. (1966). Laser Probing the Lower Atmosphere, *Nature,* Vol. 209, Iss. 5019.
doi: 10.1038/209184a0

Cooney, J. (1972). Measurement of Atmospheric Temperature Profiles by Raman Backscatter, *Journal of Applied Meteorology*, Vol. 11, Iss. 1.
doi: 10.1175/1520-0450(1972)011<0108:moatpb>2.0.co;2

DCU School of Physics Sciences. (2020). *Applied Spectroscopy.*
http://www.physics.dcu.ie/~be/Ps415/Raman-04.pdf

Di Girolamo, P., Marchese, R., Whiteman, D.N., Demoz, B.B. (2004). Rotational Raman Lidar Measurements of Atmospheric Temperature in the UV, *Geophysical Research Letters*, Vol. 31.
doi: 10.1029/2003GL018342

Elterman, L. (1953). A Series of Stratospheric Temperature Profiles Obtained with the Searchlight Technique, *Journal of Geophysical Research*, Vol. 58, Iss. 4.
doi: 10.1029/jz058i004p00519

Fernald, F.G. (1984). Analysis of Atmospheric Lidar Observations: Some Comments, *Applied Optics*, Vol. 23, Iss. 5.
doi: 10.1364/ao.23.000652

Fiocco, G., Benedetti-Michelangeli, G., Madonna, E. (1971). Measurement of Temperature and Aerosol to Molecule Ratio in the Troposphere by Optical Radar, *Nature Physical Science*, Vol. 229, Iss. 3.
doi: 10.1038/physci229078a0

Hurrell, J., Meehl, G. (2006). *Temperature Trends in the Lower Atmosphere- Understanding and Reconciling Differences*. The U.S. Climate Change Science Program and the Subcommittee on Global Change Research.

Kampfrath T., Wolf M., Sajadi M. (2018). The Sign of the Polarizability Anisotropy of Polar Molecules is Obtained from the Terahertz Kerr Effect**.** *Chemical Physics Letters,* Vol. 692. doi: 10.1016/j.cplett.2017.12.061

Klett, J. (1981). Stable Analytical Inversion Solution for Processing Lidar Returns, *Applied Optics*, Vol. 20, Iss. 2.
doi: 10.1364/ao.20.000211

La Sorte, F. A., Butchart, S. H., Böhning-Gaese, K. (2014). Range-Wide Latitudinal and Elevational Temperature Gradients for the World's Terrestrial Birds: Implications under Global Climate Change, *PLoS ONE*, Vol. 9, Iss. 5.
doi: 10.1371/journal.pone.0098361

Lading, L., Schwiesow, R. (1981). Temperature Profiling by Rayleigh-Scattering Lidar, *Applied Optics*, Vol. 20, Iss. 11.
doi: 10.1364/ao.20.001972

Lading, L., Skov Jensen, A., Schwiesow, R., Fog, C., Rasmussen, E. (1979). *Abstracts Ninth International Laser Radar Conference* [Conference report]. AMS 1979, Boston, MA, United States.

Landgraf, J., Hasekamp, O.P., van Deelen, R., and Aben, I. (2004). Rotational Raman Scattering of Polarized Light in the Earth Atmosphere: a Vector Radiative Transfer Model using the Radiative Transfer Perturbation Theory Approach, *Journal of Quantitative Spectroscopy and Radiative Transfer*, Vol. 87, 3-4.
doi: 10.1016/j.jqsrt.2004.03.013

Lee M., Lee D., Ko, E., Park, K., Kim, J., Sharma, M., Cho G. (2020). Pulse Pileup Correction Method for Gamma Ray Spectroscope in High Radiation Fields, *Nuclear Engineering and Technology*, Vol. 52, Iss. 5.
doi: 10.1016/j.net.2019.12.003

Liou, K.N. (2002). *An Introduction to Atmospheric Radiation* (2nd ed.). International Geophysics Series.

Liu, Z., Hunt, W., Vaughan, M., Hostetler, C., McGill, M., Powell, K., Winker, D., Yongxiang, H. (2006). Estimating Random Errors due to Shot Noise in Backscatter Lidar Observations, *Applied Optics*, Vol. 45, Iss. 18.

Ludwig, J. (2014). *LIDAR measurements: Determination of the aerosol extinction coefficient and comparison of incomplete overlap correction methods*. [Master thesis, University of Munich]. Meteorological Institute Munich.

Moon J. H., Jung M. (2020). Geometrical Properties of Spilled Oil on Seawater Detected Using a LiDAR Sensor, *Journal of Sensors*.
doi: 10.1155/2020/5609168

Natural Resources Canada. (2020*). Aerial LiDAR and Forest Inventory Monitoring.* Government of Canada. https://www.nrcan.gc.ca/our-natural-resources/forests-forestry/sustainable-forest-management/measuring-reporting/remote-sensing-forestry/aerial-lidar-and-forest-inventory-monitoring/13425

Northend C. A., Honey R. C., Evans W. E. (1966). Laser Radar (Lidar) for Meteorological Observation, *Review of Scientific Instruments,* Vol. 3, Iss. 4. doi: 10.1063/1.1720199

R. Gordon, Gould. (1959). The LASER, Light Amplification by Stimulated Emission of Radiation. *The Ann Arbor Conference on Optical Pumping, the University of Michigan*. 1959, Ann Arbor, MI, United States.

Rohr, T. S., Hawkins, G. J. (2015). Spectral Design of Temperature-Invariant Narrow Bandpass Filters for the Mid-Infrared, *Optics Express*, Vol. 23, Iss. 1. doi: 10.1364/OE.23.000580

Stillwell, R.A., Spuler, S. M., Hayman, M., Repasky, K.S., Bunn, C.E. (2020). Demonstration of a Combined Differential Absorption and High Spectral Resolution Lidar for Profiling Atmospheric Temperature, *Optics Express*, Vol. 28, Iss. 1. doi: 10.1364/OE.379804

Stoyanov, D., Grigorov, I., Kolarov, G., Peshev, Z., Dreischuh, T. (2012). *Advanced Photonic Sciences.* InTech.

Whiteway, J., Daly, M., Carswell, A., Duck, T., Dickinson, C., Komguem, L., Cook, C. (2008). LIDAR on the Phoenix Mars mission. *Journal of Geophysics Research E: Planets*, Vol. 114, Iss. 3.

doi: 10.1029/2007JE003002